

Paleoceanography and Paleoclimatology[®]

RESEARCH ARTICLE

10.1029/2022PA004542

Special Section:

DeepMIP in the Hothouse Earth: late Paleocene early Eocene climates and their lessons for the future

Key Points:

- The early Eocene hydrological cycle in the DeepMIP models is characterized by a “wet-gets-wetter, dry-gets-drier” response
- The early Eocene exhibits weaker subtropical moisture divergence in simulations with reduced meridional temperature gradients
- This highlights the important role of the meridional temperature gradient when predicting past (and future) rainfall patterns

Supporting Information:

Supporting Information may be found in the online version of this article.

Correspondence to:

G. N. Inglis,
gordon.inglis@soton.ac.uk

Citation:

Cramwinckel, M. J., Burls, N. J., Fahad, A. A., Knapp, S., West, C. K., Reichgelt, T., et al. (2023). Global and zonal-mean hydrological response to early Eocene warmth. *Paleoceanography and Paleoclimatology*, 38, e2022PA004542. <https://doi.org/10.1029/2022PA004542>

Received 31 AUG 2022

Accepted 25 MAY 2023

Author Contributions:

Conceptualization: Margot J. Cramwinckel, Natalie J. Burls, Gordon N. Inglis
Data curation: Margot J. Cramwinckel, Christopher K. West, Tammo Reichgelt, David R. Greenwood, Gordon N. Inglis

© 2023. The Authors.

This is an open access article under the terms of the [Creative Commons Attribution License](#), which permits use, distribution and reproduction in any medium, provided the original work is properly cited.

Global and Zonal-Mean Hydrological Response to Early Eocene Warmth

Margot J. Cramwinckel^{1,2} , Natalie J. Burls³ , Abdullah A. Fahad^{3,4}, Scott Knapp³ , Christopher K. West^{5,6} , Tammo Reichgelt⁷ , David R. Greenwood⁸ , Wing-Le Chan⁹ , Yannick Donnadieu¹⁰ , David K. Hutchinson¹¹ , Agatha M. de Boer¹² , Jean-Baptiste Ladant¹³ , Polina A. Morozova¹⁴, Igor Niegzodzki^{15,16}, Gregor Knorr¹⁶ , Sebastian Steinig¹⁷ , Zhongshi Zhang¹⁸ , Jiang Zhu¹⁹ , Ran Feng⁷ , Daniel J. Lunt¹⁷ , Ayako Abe-Ouchi⁹ , and Gordon N. Inglis¹ 

¹School of Ocean and Earth Science, University of Southampton, Southampton, UK, ²Now at Department of Earth Sciences, Utrecht University, Utrecht, The Netherlands, ³Department of Atmospheric, Oceanic and Earth Sciences, Center for Ocean-Land-Atmosphere Studies, George Mason University, Fairfax, VA, USA, ⁴GMAO, NASA Goddard Space Flight Center, Greenbelt, MD, USA, ⁵Department of Earth and Atmospheric Sciences, University of Alberta, Edmonton, AB, Canada, ⁶Now at Royal Tyrrell Museum of Palaeontology, Drumheller, AB, Canada, ⁷Department of Earth Sciences, University of Connecticut, Storrs, CT, USA, ⁸Department of Biology, Brandon University, Brandon, MB, Canada, ⁹Atmosphere and Ocean Research Institute, University of Tokyo, Kashiwa, Japan, ¹⁰Aix Marseille University, CNRS, IRD, INRA, Coll France, CEREGE, Aix-en-Provence, France, ¹¹Climate Change Research Centre, University of New South Wales Sydney, Sydney, Australia, ¹²Department of Geological Sciences, Stockholm University, Stockholm, Sweden, ¹³Laboratoire des Sciences du Climat et de l'Environnement, LSCE/IPSL, CEA-CNRS-UVSQ, Université Paris-Saclay, Gif-sur-Yvette, France, ¹⁴Institute of Geography, Russian Academy of Sciences, Moscow, Russia, ¹⁵Institute of Geological Sciences Polish Academy of Sciences, Kraków, Poland, ¹⁶Alfred Wegener Institute for Polar and Marine Research, Bremerhaven, Germany, ¹⁷School of Geographical Sciences, University of Bristol, Bristol, UK, ¹⁸Bjerknes Centre for Climate Research, University of Bergen, Bergen, Norway, ¹⁹National Center For Atmospheric Research, Boulder, CO, USA

Abstract Earth's hydrological cycle is expected to intensify in response to global warming, with a “wet-gets-wetter, dry-gets-drier” response anticipated over the ocean. Subtropical regions ($\sim 15^{\circ}$ – 30° N/S) are predicted to become drier, yet proxy evidence from past warm climates suggests these regions may be characterized by wetter conditions. Here we use an integrated data-modeling approach to reconstruct global and zonal-mean rainfall patterns during the early Eocene (~ 56 – 48 million years ago). The Deep-Time Model Intercomparison Project (DeepMIP) model ensemble indicates that the mid- (30° – 60° N/S) and high-latitudes ($>60^{\circ}$ N/S) are characterized by a thermodynamically dominated hydrological response to warming and overall wetter conditions. The tropical band (0° – 15° N/S) is also characterized by wetter conditions, with several DeepMIP models simulating narrowing of the Inter-Tropical Convergence Zone. However, the latter is not evident from the proxy data. The subtropics are characterized by negative precipitation-evaporation anomalies (i.e., drier conditions) in the DeepMIP models, but there is surprisingly large inter-model variability in mean annual precipitation (MAP). Intriguingly, we find that models with weaker meridional temperature gradients (e.g., CESM, GFDL) are characterized by a reduction in subtropical moisture divergence, leading to an increase in MAP. These model simulations agree more closely with our new proxy-derived precipitation reconstructions and other key climate metrics and imply that the early Eocene was characterized by reduced subtropical moisture divergence. If the meridional temperature gradient was even weaker than suggested by those DeepMIP models, circulation-induced changes may have outcompeted thermodynamic changes, leading to wetter subtropics. This highlights the importance of accurately reconstructing zonal temperature gradients when reconstructing past rainfall patterns.

Plain Language Summary As the world warms, the atmosphere is able to hold more moisture—however, this moisture will not fall evenly across the globe. Some regions are expected to become wetter, whereas other regions will become drier. This is the basis of the familiar paradigm “wet-gets-wetter, dry-gets-drier” and is largely supported by future model projections. However, evidence from the geological record contradicts this hypothesis and suggests that a warmer world could be characterized by wetter (rather than drier) subtropics. Here, we use an integrated data-modeling approach to investigate the hydrological response to warming during an ancient warm interval (the early Eocene, 56–48 million years ago). We show that models with weaker latitudinal temperature gradients are characterized by a reduction in subtropical

Formal analysis: Margot J. Cramwinckel, Natalie J. Burls, Abdullah A. Fahad, Scott Knapp, Christopher K. West, Tammo Reichgelt, David R. Greenwood

Funding acquisition: Gordon N. Ingis

Methodology: Margot J. Cramwinckel, Natalie J. Burls, Abdullah A. Fahad, Scott Knapp, Christopher K. West, Tammo Reichgelt, David R. Greenwood, Wing-Le Chan, Yannick Donnadieu, David K. Hutchinson, Jean-Baptiste Ladant, Polina A. Morozova, Igor Niezgodzki, Sebastian Steinig, Zhongshi Zhang, Jiang Zhu, Ayako Abe-Ouchi

Software: Natalie J. Burls, Abdullah A. Fahad, Scott Knapp

Supervision: Natalie J. Burls, Gordon N. Ingis

Visualization: Margot J. Cramwinckel, Natalie J. Burls, Gordon N. Ingis

Writing – original draft: Margot J. Cramwinckel

Writing – review & editing: Margot J. Cramwinckel, Natalie J. Burls, Abdullah A. Fahad, Scott Knapp, Christopher K. West, Tammo Reichgelt, David R. Greenwood, Wing-Le Chan, Yannick Donnadieu, David K. Hutchinson, Agatha M. de Boer, Jean-Baptiste Ladant, Polina A. Morozova, Igor Niezgodzki, Sebastian Steinig, Zhongshi Zhang, Jiang Zhu, Ran Feng, Daniel J. Lunt, Gordon N. Ingis

moisture divergence. However, this was not sufficient to induce subtropical wetting. If the meridional temperature gradient was weaker than suggested by the models, circulation-induced changes may have lead to wetter subtropics. This work shows that the latitudinal temperature gradient is a key factor that influences hydroclimate in the subtropics, especially in past warm climates.

1. Introduction

Future global warming is projected to be associated with a global-mean increase in mean annual precipitation (MAP) and a shift in regional and seasonal rainfall patterns (Chapter 8 of Masson-Delmotte et al., 2022), with important consequences for societies and ecosystems. Under higher global temperatures, Earth's atmosphere will contain more water vapor following the Clausius–Clapeyron relation (Held & Soden, 2006). This “thermodynamic effect” forms the basis for the predicted zonal-mean “wet-gets-wetter, dry-gets-drier” response under enhanced radiative forcing, whereby the existing spatial patterns in precipitation-evaporation ($P-E$) are exacerbated over the ocean (Held & Soden, 2006; Seager et al., 2010). However, this simple thermodynamic scaling does not hold true over land (Byrne & O’Gorman, 2015) and dynamical processes likely play an additional role (Byrne & O’Gorman, 2015). Overall, general circulation models (GCMs) used in Coupled Model Intercomparison Project Phase 6 (CMIP6) suggest that higher global mean surface temperatures (GMST) will lead to wetter high latitudes ($>60^{\circ}\text{N/S}$) (i.e., positive $P-E$ change), and drier subtropics ($15^{\circ}\text{--}30^{\circ}\text{N/S}$) (i.e., negative $P-E$ change) (Hoegh-Guldberg et al., 2018; Masson-Delmotte et al., 2022). However, the same models disagree on the nature of change in much of the remainder of the low to middle latitudes, both over land and ocean (Masson-Delmotte et al., 2022; Slingo et al., 2022), which is a key uncertainty for appropriate climate mitigation and adaptation.

Moreover, evidence from warm intervals in the geological past suggests that the subtropics may ultimately get wetter (rather than drier) under quasi-equilibrated warmer conditions, that is, “dry-gets-wetter.” For example, both the Miocene (23.0–5.3 million years ago; Ma) and Pliocene (5.3–2.6 Ma) yield multi-proxy evidence for wetter subtropics in southern Australia (Sniderman et al., 2016), North Africa (Feng et al., 2022; Hailemichael et al., 2002; Schuster et al., 2009), South America (Carrapa et al., 2019), South-East Asia (Feng et al., 2022; Wang et al., 2019), and western North American (Bhattacharya et al., 2022). Burls and Fedorov (2017) suggest these wetter subtropical conditions were due to weaker large-scale surface temperature gradients supporting weaker large-scale atmospheric circulation and hence subtropical moisture divergence. Although the impact of zonal-mean changes in circulation (dynamic effect) is often considered secondary to changes in atmospheric humidity (thermodynamic effect), the former may be important under certain climate scenarios (e.g., weak latitudinal temperature gradients; LTGs; see also Byrne & O’Gorman, 2015) and may even compensate for an increase in atmospheric humidity (Burls & Fedorov, 2017). At a regional scale, enhanced monsoonal circulation in the north Africa–east Asia region (Feng et al., 2022; Zhang et al., 2013) and western North America (Bhattacharya et al., 2022) further account for the wetter climate across those subtropical monsoon regions.

Here we focus on the early Eocene (56.0–47.8 million years ago; Ma) (Hollis et al., 2019), an interval characterized by higher CO_2 values ($>1,000$ parts per million) (Anagnostou et al., 2020), higher global mean surface temperature ($10\text{--}16^{\circ}\text{C}$ warmer than pre-industrial) (Ingis et al., 2020) and reduced pole-to-equator LTGs (of $\sim 17^{\circ}\text{--}22^{\circ}\text{C}$) (Cramwinckel et al., 2018; Evans et al., 2018; Gaskell et al., 2022). This is an ideal interval to study how changes in GMST and the LTG impact tropical, subtropical, mid- and high-latitude rainfall patterns. However, there are very few quantitative early Eocene-aged MAP estimates, particularly from the subtropics ($15^{\circ}\text{--}30^{\circ}\text{N/S}$), and the hydrological response to warming remains largely unknown. To resolve this, we utilize the recently published state-of-the-art Deep-Time Model Intercomparison Project (DeepMIP) suite of Eocene model simulations (Lunt et al., 2021) to explore the simulated global- and regional-scale hydrological response to warming. This is combined with a new (terrestrial) proxy compilation to answer the following questions: (a) How does simulated tropical, subtropical, mid- and high-latitude MAP and $P-E$ respond to Eocene boundary conditions and increasing GMST, and what is the level of agreement across the DeepMIP models? (b) What is the relative role of changes in local evaporation versus moisture divergence (time-mean and eddy) in driving the MAP changes? (c) Are early Eocene simulations characterized by a “wet-gets-wetter, dry-gets-drier” response? (d) How do the simulated thermodynamic (i.e., humidity) and dynamic (i.e., circulation) effects contribute to changes in moisture transport in the subtropics? (e) How well do the DeepMIP models replicate proxy-derived MAP estimates?

2. Methods

2.1. Modeling Simulations

2.1.1. DeepMIP-Eocene Simulations

We make use of the DeepMIP suite of model simulations, embedded in the fourth phase of the Paleoclimate Modeling Intercomparison Project (Kageyama et al., 2018), itself a part of the sixth phase of the Coupled Model Intercomparison Project (CMIP6; Eyring et al., 2016). An extensive description of the standard design of these model experiments is provided in Lunt et al. (2017), and an overview of the large-scale climate features has been presented in Lunt et al. (2021). The main advantage of these simulations over the EoMIP (Eocene Modeling Intercomparison Project) “ensemble of opportunity” employed in earlier work (Carmichael et al., 2016) is that the new DeepMIP simulations have been designed and carried out using internally consistent Eocene boundary conditions (Herold et al., 2014; Lunt et al., 2017). Simulations have been run at different atmospheric CO₂ levels—typically $\times 1$, $\times 3$, $\times 6$, and $\times 9$ preindustrial (PI) CO₂, but with a subset of these, or additional atmospheric CO₂ concentrations, chosen by some model groups (see Lunt et al., 2017; Lunt et al., 2021). Different CO₂ experiments are expected to provide comparison targets to climate reconstructions for different key time slices, including the early Eocene Climatic Optimum (EECO; ~ 53.3 – 49.1 Ma), the Paleocene–Eocene Thermal Maximum (PETM; ~ 56 Ma), and the latest Paleocene (i.e., pre-PETM). Pre-industrial simulations ($\times 1$ CO₂) with modern continental configurations have also been performed to assess the influence of non-CO₂ Eocene boundary conditions. Simulations have been performed with eight different models (Table S1 in Supporting Information S1) and detailed descriptions of the models and simulations are provided in Lunt et al. (2021). To explore regional variations in hydroclimate, we subdivide our data into four latitudinal bands: (a) the tropics (0°–15°N/S), (b) the subtropics (15°–30°N/S), (c) the mid-latitudes (30°–60°N/S), and (d) the high-latitudes (>60 °N/S). To further deconvolve the cause of global and regional variations, we perform a moisture budget analysis. The analyzed climatologies are based on the last 100 years of each simulation. As different models provided slightly different variables, for some models we were not able to provide analysis of *P*–*E* (NorESM), or moisture budget analysis (IPSL, INMCM, and NorESM). We compare observed changes in subtropical hydrology to changes in the modeled latitudinal temperature gradient (LTG), here taken as the difference in surface temperature between the mid-latitudes (30°–60°N/S) and the tropics (15°N–15°S).

2.1.2. Moisture Budget Analysis

To diagnose the cause of *P*–*E* changes within the DeepMIP ensemble, we conduct a moisture budget analysis (Seager & Henderson, 2013; Trenberth & Guillemot, 1995). This approach relies on the fact that climatological changes in *P*–*E*—calculated over a long enough timescale that fluctuations in the column integrated moisture content are negligible (in our case the last 100 years of each DeepMIP simulation)—are balanced by the column-integrated convergence of moisture in the overlying atmosphere, as follows:

$$P - E = -\nabla \cdot \frac{1}{g} \int_{p_t}^{p_s} \vec{v} q \, dp$$

where *g* is the acceleration due to gravity (ms⁻²), *q* the atmospheric specific humidity (kg/kg), and *v* the horizontal wind vector (ms⁻¹) integrated across pressure (*p*, Pa) levels from the surface (*p_s*) to the top of the troposphere (tropopause; *p_t*). This climatological moisture convergence can be further decomposed into its time-mean ($\bar{v} \bar{q}$) and eddy ($v' q'$) components. The time-mean component is calculated using the climatological mean data provided in the DeepMIP data set while the eddy component is calculated as the residual between *P*–*E* and the time-mean component given that the high temporal resolution data required to calculate this term explicitly is not available as part of the DeepMIP data set.

2.2. Proxy Synthesis

2.2.1. Approach

Fossil leaves and palynomorphs (spores and pollen) can provide quantitative estimates of MAP in the past. Using these, the primary approaches are: (a) leaf physiognomy (i.e., leaf shape) (Givnish, 1984; Greenwood, 2007; Wing & Greenwood, 1993; Wolfe, 1993) and (b) nearest living relative (NLR)-based approaches (Greenwood et al., 2003; Pancost et al., 2013; Pross et al., 2000; Suan et al., 2017; West et al., 2020). A multi-proxy approach

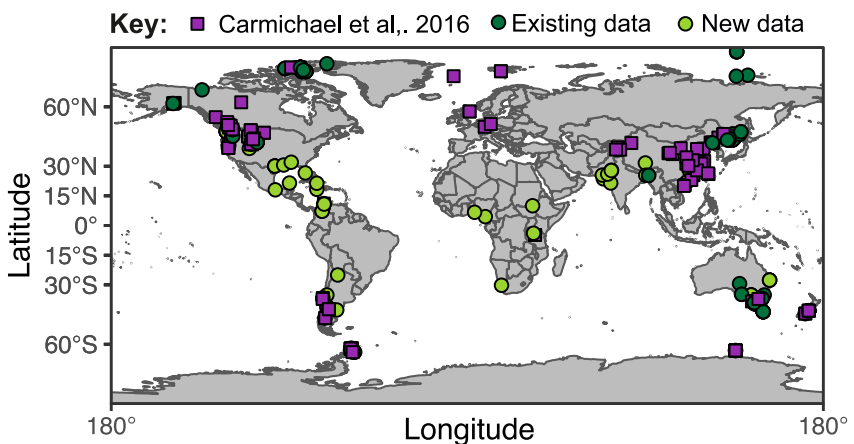


Figure 1. Overview of early Eocene precipitation proxy compilation. Previously published estimates compiled by Carmichael et al. (2016) shown as purple squares; additional published estimates plotted as dark green circles; new estimates (*this study*) plotted as light green circles. Sample locations plotted with their modern positions on a present-day world map.

combining leaf physiognomy and NLR data is generally recommended and mitigates the different uncertainties incorporated by individual approaches (e.g., West et al., 2020).

Methods based on leaf physiognomy utilize the correlation between the architecture of leaves and climatic variables. As leaf size and shape are highly sensitive to moisture availability (Givnish, 1984; Peppe et al., 2011; Spicer et al., 2021), fossil leaf architecture can be related to precipitation using univariate methods such as Leaf Area Analysis (LAA) (Wilf et al., 1998). The Climate Leaf Analysis Multivariate Program (CLAMP) (Wolfe, 1993, 1995) combines multiple leaf traits, including leaf area, leaf shape, and margin state (i.e., toothed or untoothed), to provide estimates of annual and seasonal precipitation (Spicer et al., 2021). Anatomical characteristics of fossil wood can likewise reflect climate variables (Poole and van Bergen, 2006; Wiemann et al., 1998). Although wood anatomy as a climate proxy has not had widespread application in deep time climate compilations, multivariate models of various wood anatomical characters are typically used (e.g., Poole et al., 2005).

NLR approaches are based on the premise that the climatic tolerance of a paleo-vegetation assemblage can be inferred from their presumed extant relatives (e.g., Fauquette et al., 1998; Greenwood et al., 2003; Mosbrugger & Utescher, 1997; West et al., 2020; Willard et al., 2019). These methods can be based on macrofossil (most often leaf fossils but also seeds, fruits, or wood) or microfossil (i.e., sporomorphs) paleobotanical assemblages, as long as the taxa can be correlated to a living relative with a known climatic tolerance. The coexistence approach (CA; Mosbrugger & Utescher, 1997) is a specific instance of this, in which the single climatic interval in which all NLRs can coexist is reconstructed. More recent studies employing Bioclimatic Analysis (BA) typically calculate probability density functions of climatic variables instead of minimum-to-maximum intervals (e.g., West et al., 2020; Willard et al., 2019). The Climatic Amplitude Method (CAM) is an alternative NLR approach that incorporates relative abundances of different taxa (Fauquette et al., 1998).

2.2.2. Proxy Compilation

Here we compile paleobotanical MAP estimates for the late Paleocene (59.2–56 Ma; Thanetian) to early Eocene (56.0–47.8 Ma; Ypresian). Our compilation builds upon previous EECO- (Carmichael et al., 2016) and PETM-aged (Carmichael et al., 2017) compilations. We supplement this with (a) published MAP estimates generated since, and (b) newly generated MAP estimates using CLAMP and NLR on published palynological and macrofloral (predominantly leaf-based) datasets. Our new proxy synthesis ($n = 322$) contains 133 MAP estimates (41%) from Carmichael et al. (2016), 106 data points (33%) from other published sources, and 83 new data points (26%) (Figure 1; Tables S1 and S2 in Supporting Information S1). The new data in the compilation helps to improve geographical coverage in previously data-poor regions, including central west coast and eastern Africa (e.g., Adeonipekun et al., 2012; Cantrill et al., 2013; Eisawi & Schrank, 2008) (also recently presented in Williams et al. (2022)); the coal and lignite bearing deposits of northeastern India and southern Pakistan (Frederiksen, 1994; Tripathi et al., 2000; Verma et al., 2019); the Tibetan plateau and sedimentary basins of southern China (e.g., Aleksandrova et al., 2015; Su et al., 2020; Xie et al., 2020); and the South American (e.g., Jaramillo et al., 2007;

Pardo-Trujillo et al., 2003; Quattroccchio & Volkheimer, 2000) and North American continent and Caribbean islands (e.g., Graham et al., 2000; Jarzen & Klug, 2010; Smith et al., 2020) (Figure 1; Supporting Information S1). Most of these use the NLR approach based on palynological datasets, as plant macrofossils from the late Paleocene—early Eocene low latitudes are more rarely preserved, although some exceptions are known (Herman et al., 2017; Shukla et al., 2014; Wing et al., 2009). We also incorporate data from the mid and high latitudes, for example, southern South America, North America, Australia and New Zealand, and high Siberia (Supporting Information S1). For regions with exceptionally poor data coverage (e.g., tropical and subtropical latitudes, Antarctica), we also compile and generate MAP estimates from the early middle Eocene (47.8–45 Ma; first half of the Lutetian). Published CLAMP and NLR data were re-analyzed following recent recommendations, so that there is no bias as a result of discrepant methodology. Specifically, (a) CLAMP-scored fossil leaf assemblages were re-analyzed using up-to-date geographically appropriate calibration datasets (Kennedy et al., 2014; Reichgelt et al., 2019; Yang et al., 2015), (b) for both CLAMP and NLR reconstructions, gridded climate datasets from the R package dismo were employed (Hijmans et al., 2020), and (c) NLR analysis was performed using consistently filtered modern distribution datasets to avoid regional overrepresentation (e.g., West et al., 2020). Modern site coordinates and age constraints were extracted from the original publications.

2.2.3. Data-Model Comparison Framework

To compare proxy and model data, we employ a data comparison similar to that used for the Miocene MioMIP ensemble (Burls et al., 2021). This approach requires inclusion of uncertainty for both the proxy and model MAP estimates. To account for site location uncertainty, we determine site co-ordinates for the age range of our proxy data compilation above, that is, from 59 Ma (late Paleocene) to 45 Ma (early middle Eocene) using the Müller et al. (2016) Gplates continental polygons in combination with the hotspot-based rotation frame of Matthews et al. (2016) (i.e., analogous to all DeepMIP simulations apart from NorESM; Lunt et al., 2020). For the model simulations, MAP values are taken from the grid cells that fall within the proxy location uncertainty. The model MAP uncertainty is subsequently defined as the range between minimum and maximum MAP within these model grid cells. For proxy estimates, we use the proxy error and error type as reported in the original study. Typically, this is a minimum–maximum range or confidence interval (e.g., 95%) for NLR approaches (e.g., West et al., 2020; Willard et al., 2019), and standard error (SE) or standard deviation (SD) derived from calibration data set residuals for leaf physiognomy methods (e.g., Teodoridis et al., 2011). For our newly generated values, uncertainties are reported as 95% confidence interval for NLR and ± 1 SD for CLAMP. The subsequent overlap between the model and proxy uncertainty range is assessed following the MioMIP methodology (Burls et al., 2021). Any overlap between the proxy and model uncertainty ranges is defined as “no bias” (Figure S1 in Burls et al., 2021).

3. Results and Discussion

3.1. DeepMIP Models Reproduce Pre-Industrial Global Precipitation Patterns

Each model included in the DeepMIP suite is able to reproduce the main features of pre-industrial precipitation patterns (Figure 2, Figure S1 in Supporting Information S1). However, some common model precipitation biases are apparent. For example, all simulations exhibit a double Inter-Tropical Convergence Zone (ITCZ) in MAP, simulating excess precipitation south of the equator. This bias is common and the double ITCZ remains a consistent error in both the previous (e.g., CMIP3, CMIP5) and latest (CMIP6) generation of climate models (Tian & Dong, 2020). There is also a lack of simulated precipitation in the western equatorial Pacific (Figure 2c). Never-the-less, the shape of the South Pacific convergence zone (SPCZ) is improved in the multi-model mean (MMM) compared to the previous EoMIP generation model simulations (Carmichael et al., 2016).

3.2. Influence of Non-CO₂ Boundary Conditions on the Early Eocene Hydrological Cycle

Non-CO₂ boundary conditions (i.e., paleogeography, vegetation, aerosols) can exert an influence on global and regional MAP and *P*–*E* values. The previous EoMIP ensemble found a minor role for non-CO₂ boundary conditions on global MAP (+0.1 mm/day; Carmichael et al., 2016). However, this analysis was only performed for a single model simulation (HadCM3L). To better isolate the influence of non-CO₂ boundary conditions on the early Eocene hydrological cycle, we compared early Eocene 1x CO₂ simulations and pre-industrial 1x CO₂ simulations from multiple ($n = 6$) DeepMIP models.

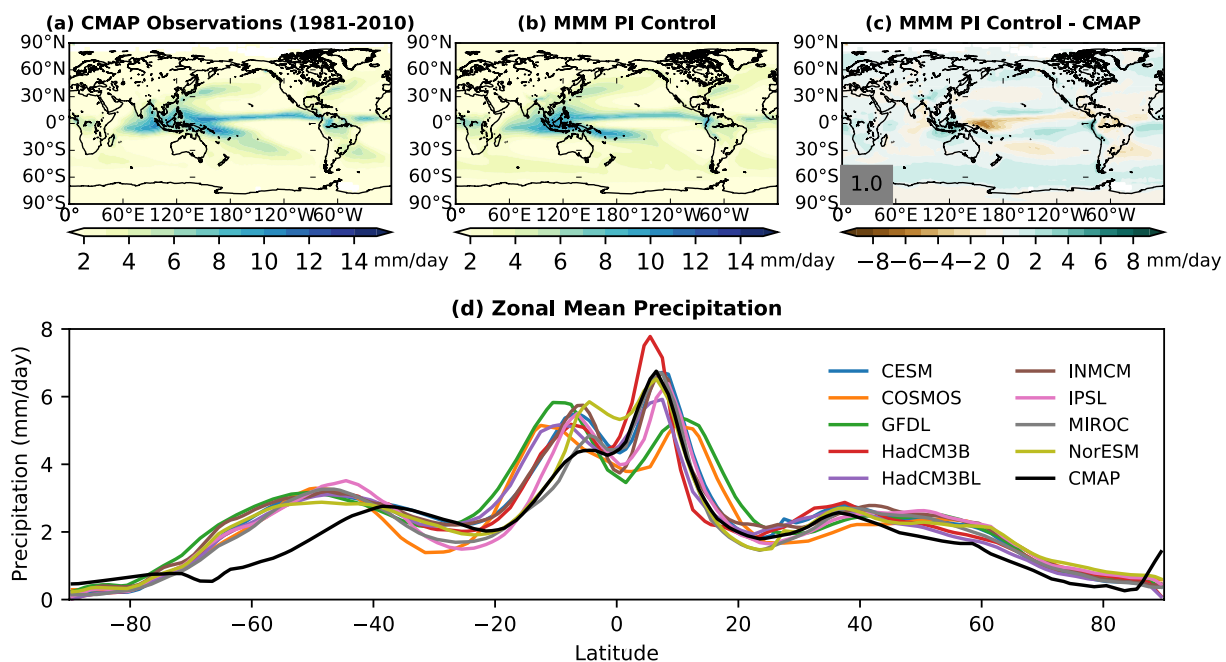


Figure 2. Rainfall patterns in Deep-Time Model Intercomparison Project (DeepMIP) pre-industrial simulations. (a) Climate Prediction Center (CPC) Merged Analysis of Precipitation (CMAP) Observations (Xie & Arkin, 1997), (b) multi-model mean (MMM) of precipitation estimates (mm/day) for the pre-industrial control runs for the 99 model simulations in the DeepMIP ensemble (middle), (c) MMM anomalies in precipitation (mm/day) for DeepMIP pre-industrial control runs minus modern observations. (d) Zonal-mean precipitation of DeepMIP model control runs and modern observations. Note that the MMM contains a different model ensemble for different CO_2 concentrations (see Figure 4 and Table S1 in Supporting Information S1).

At a global scale, the early Eocene $1\times \text{CO}_2$ simulations are characterized by higher MAP values relative to pre-industrial (0.1–0.4 mm/day; $1\times \text{CO}_2$ symbols in Figure 3). This is because the early Eocene $1\times \text{CO}_2$ simulations have higher global mean surface temperatures ($\sim 3\text{--}5^\circ\text{C}$) relative to the preindustrial $1\times \text{CO}_2$ control simulations (see also Lunt et al., 2021) (Figure S2 in Supporting Information S1).

This leads to enhanced surface evaporation which is balanced by precipitation globally (Held & Soden, 2006; Siler et al., 2019).

At a regional scale, the early Eocene $1\times \text{CO}_2$ simulations are characterized by higher MAP estimates in the tropics ($0\text{--}15^\circ\text{N/S}$), mid-latitudes ($30\text{--}60^\circ\text{N/S}$), and high-latitudes ($>60^\circ\text{N/S}$) (typically $+0.1$ to $+0.4$ mm/day, but up to $+0.6$ mm/day in the high-latitudes, Figures 4 and 5; Figure S3 in Supporting Information S1) relative to pre-industrial. The tropics, mid-latitudes, and high-latitudes are also characterized by positive $P-E$ values (typically $+0.1\text{--}0.2$ mm/day, but up to $+0.4$ mm/day in the high-latitudes; Figures 4 and 6 and Figures S4 and S5 in Supporting Information S1) relative to pre-industrial. Furthermore, the tropics are characterized by an eastward shift and expansion in deep tropical convection, and hence the Walker Circulation, over the Pacific Ocean (Figure 4). Focusing on the ITCZ, non- CO_2 Eocene boundary conditions only affect the width of the ITCZ (defined as in Byrne and Schneider (2016)) in CESM and MIROC, where it increases slightly (Figure 7a). Additionally, the ITCZ latitude of maximum precipitation shifts northwards relative to the preindustrial control in three (CESM, HadCM3B, and MIROC) of the five models that performed the $1\times \text{CO}_2$ experiment (Figure 7b). The subtropical ($15\text{--}30^\circ\text{N/S}$) early Eocene $1\times \text{CO}_2$ MMM difference from the pre-industrial is characterized by negative $P-E$ values (-0.2 to -0.8 mm/day; Figure 6 and Figures S4 and S5 in Supporting Information S1), but the associated MAP estimates span a wide range and can be higher (i.e., CESM, GFDL, MIROC; 0.1–0.6 mm/day) or lower (i.e.,

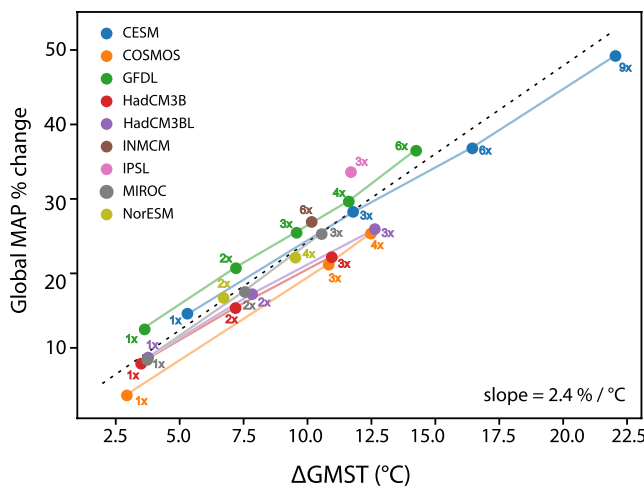


Figure 3. Global hydrological response to warming in the Deep-Time Model Intercomparison Project (DeepMIP) experiments. Global mean change in precipitation relative to pre-industrial (in % change) on the vertical axis plotted against global mean surface air temperature (GMST) relative to pre-industrial (in $^\circ\text{C}$) on the horizontal axis. Simulations with the same model at three or more different CO_2 levels have been connected by colored lines. Correlation coefficient of a linear fit through the combined values (black line) is 0.96, slope is 2.4% increase in precipitation per $^\circ\text{C}$ of warming.

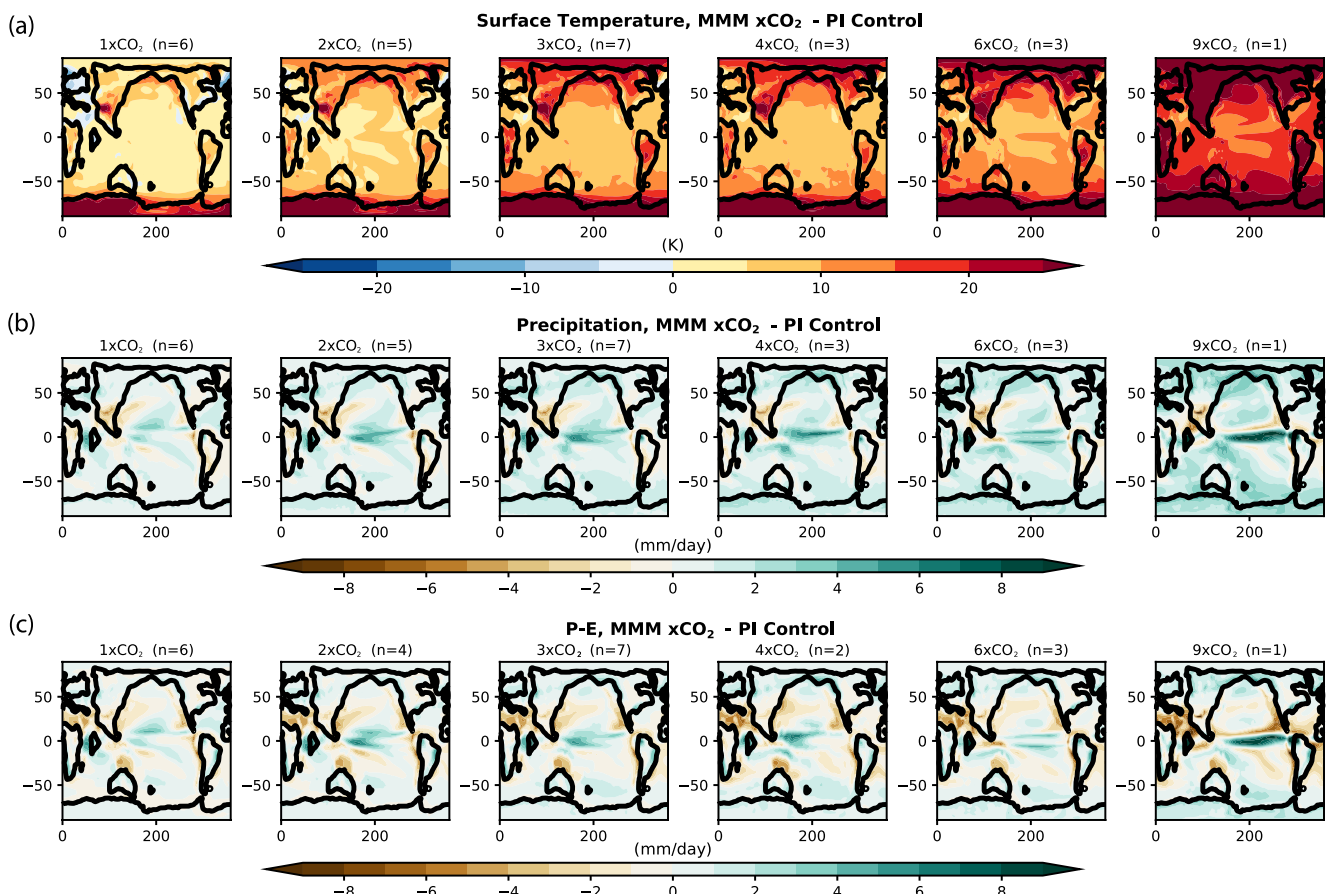


Figure 4. Multi-model mean temperature and precipitation anomalies relative to the pre-industrial control in the Deep-Time Model Intercomparison Project (DeepMIP) simulations. (a) surface air temperature, (b) precipitation and (c) precipitation—evaporation ($P-E$). “ n ” values above each plot represent the number of models available for calculating the multi-model mean. See Figure S7 in Supporting Information S1 for the standard deviation in each variable across the ensemble members contributing to the ensemble mean.

COSMOS, HadCM3L, HadCM3LB; -0.1 to -0.2 mm/day) relative to pre-industrial (Figure 5 and Figure S3 in Supporting Information S1). When assessing the relative roles of local evaporation, time-mean moisture transport divergence, and eddy moisture transport divergence changes, generally the models with increased $1\times\text{CO}_2$ subtropical MAP (i.e., CESM, GFDL, MIROC) experience increased local subtropical evaporation that is not completely counteracted by the enhanced time-mean moisture divergence (Figure 8c and Figure S6b in Supporting Information S1).

3.3. Global and Zonal-Mean Variability in the Early Eocene Hydrological Cycle

The DeepMIP simulations span a wide range of CO_2 concentrations ($x1$ to $x9$ PI CO_2) and GMST (~ 17 – 35°C) and can thus provide insights into the global- and regional-scale hydrological response to CO_2 -induced warming. Across the DeepMIP ensemble, higher GMST estimates are associated with higher global-mean MAP estimates as warming leads to enhanced surface evaporation, both between different models and within the same model at different CO_2 levels (Figure 3). Similar to previous studies (e.g., Held & Soden, 2006; Siler et al., 2019) and the latest CMIP models (MMM = $2.51\%/\text{K}$ with a range of 2.1% – $3.1\%/\text{K}$ per Pendergrass, 2020) the best linear fit across the entire DeepMIP ensemble is a 2.4% increase in global MAP per degree of warming.

Next to this global perspective, there are also zonal-mean variations in MAP that differ in their relationship with GMST (Figure 5). In the tropics (0° – 15°N/S), the mid-latitudes (30° – 60°N/S) and the high-latitudes ($>60^\circ\text{N/S}$), higher GMST estimates are associated with higher MAP estimates, with the greatest sensitivity to GMST in the high latitudes (9.1% increase in precipitation per $^\circ\text{C}$ warming; Figure 5d). As CO_2 , and hence GMST increases, both enhanced local evaporation and time-mean moisture convergence are responsible for the rise in tropical

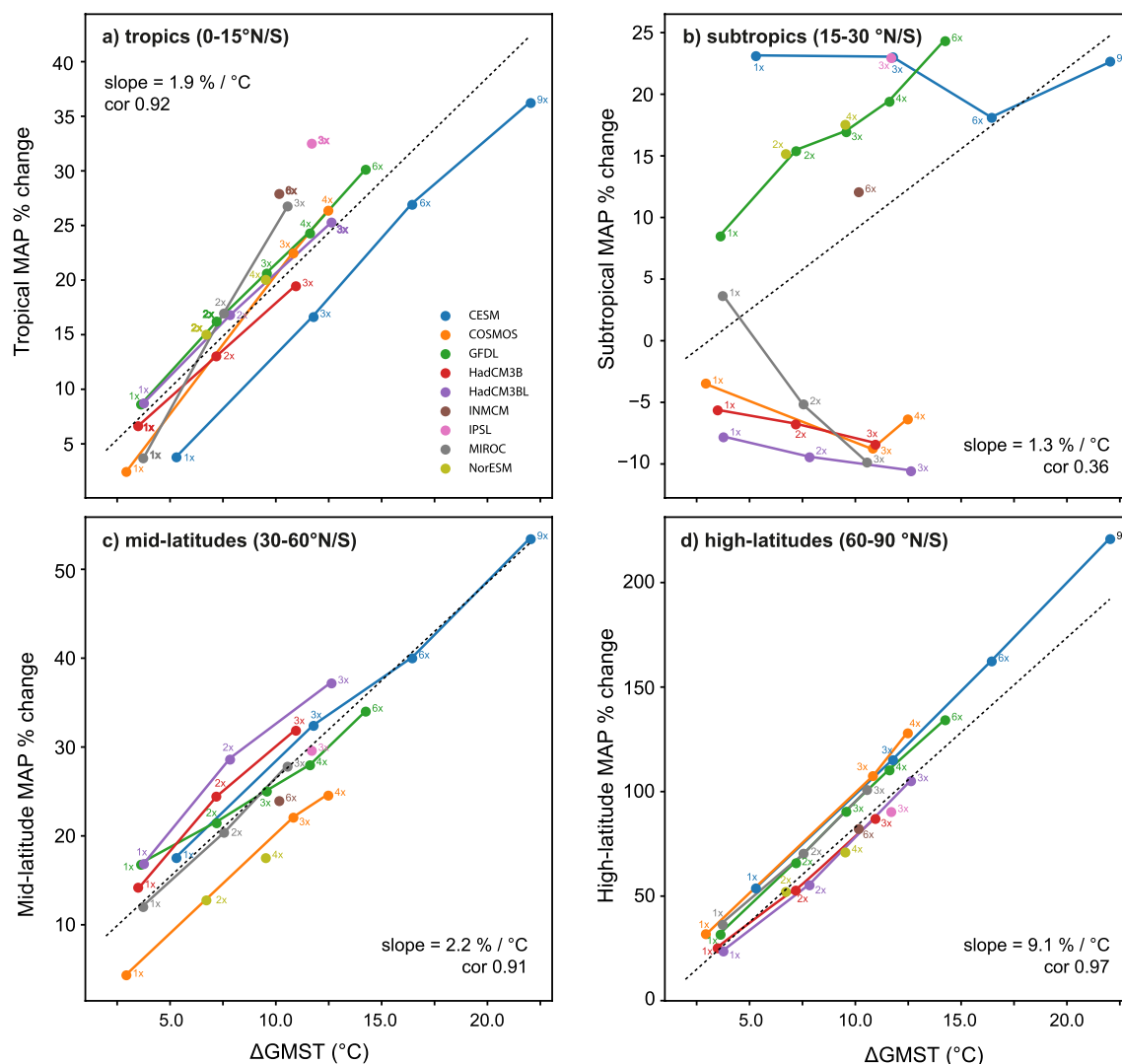


Figure 5. Mean annual precipitation (MAP) values in the Deep-Time Model Intercomparison Project (DeepMIP) Eocene simulations for the (a) tropics (15° – 15° N/S), (b) subtropics (15° – 30° N/S), (c) mid latitudes (30° – 60° N/S), and (d) high latitudes (60° – 90° N/S). Panels (a–d) show the % change in MAP relative to pre-industrial versus the change in global mean surface air temperature change (GMST; °C) relative to pre-industrial. Simulations with the same model at three or more different CO_2 levels have been connected by colored lines. Dashed black line represents a linear fit through the combined values and the slope and correlation coefficient are shown in bottom right hand corner. Note that y-axis scaling differs between plots.

precipitation across the DeepMIP multi-model ensemble (Figure S6a in Supporting Information S1). The width of the ITCZ decreases with increased CO_2 in five (CESM, COSMOS, HadCM3B, HadCM3BL and MIROC) of the six models that provided the meridional wind field variable required to perform ITCZ width calculations (Figure 7a). This is consistent with recent data-assimilation based work focusing on the PETM (Tierney et al., 2022). To varying degrees, the ITCZ latitude of maximum precipitation shifts southwards with increasing CO_2 in most of the models (Figure 7b). In the high-latitudes, increased local evaporation and time-mean plus eddy moisture convergence work together to maintain the greatest sensitivity of MAP to GMST in the high latitudes (Figure S6d in Supporting Information S1). Similar to the tropics and high-latitudes, increased local evaporation with elevated CO_2 concentrations plays a key role in increasing mid-latitude MAP values. However, much like the subtropics discussed next, there are significant model differences in the (relatively minor) contribution of the time-mean and eddy moisture flux divergence terms (Figure S6c in Supporting Information S1).

In the subtropics (15° – 30° N/S), the relationship between GMST and MAP differs greatly between the DeepMIP model simulations. For this latitudinal band there is a wide range in MAP estimates: HadCM3, MIROC and COSMOS simulate lower MAP values relative to pre-industrial, whereas CESM and GFDL simulate higher

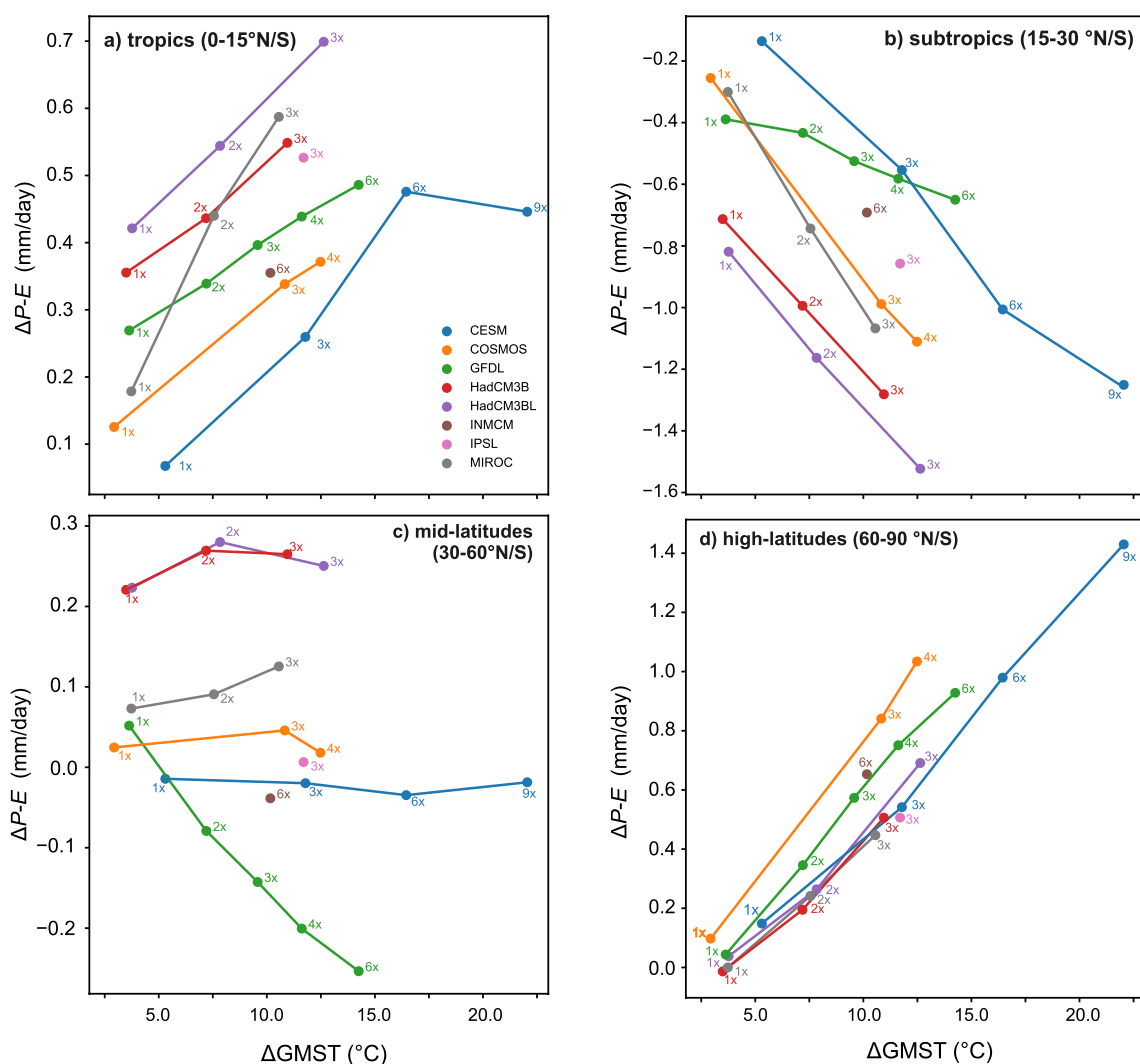


Figure 6. Precipitation-evaporation ($P-E$) values in the Deep-Time Model Intercomparison Project (DeepMIP) model simulations for the (a) tropics ($15^{\circ}-15^{\circ}\text{N/S}$), (b) subtropics ($15^{\circ}-30^{\circ}\text{N/S}$), (c) mid latitudes ($30^{\circ}-60^{\circ}\text{N/S}$), and (d) high latitudes ($60^{\circ}-90^{\circ}\text{N/S}$). Panels (a–d) show the change in $P-E$ relative to pre-industrial (mm/day) versus the change in global mean surface air temperature change (GMST; $^{\circ}\text{C}$) relative to pre-industrial. Simulations with the same model at three or more different CO_2 levels have been connected by colored lines. Note that y-axis scaling differs between plots.

MAP values relative to pre-industrial (Figure 5b). Moisture budget diagnostics (see below) suggest that a weaker latitudinal temperature gradient is the cause of higher subtropical MAP values in both CESM and GFDL.

For a given global mean temperature change, the DeepMIP models also exhibit different zonal-mean $P-E$ responses. In the tropics and the high-latitudes, higher GMST estimates are associated with more positive $P-E$ values and overall wetter conditions (Figure 6). In the subtropics, higher GMST estimates are associated with more negative $P-E$ values and overall drier conditions (Figure 6b). This indicates that from a zonal-mean perspective the early Eocene largely conforms to the “wet-gets-wetter, dry-gets-drier” hypothesis within the DeepMIP simulations. Lastly, there is a weak relationship between GMST and $P-E$ values in the mid-latitudes (Figure 6c). As the mid-latitude band encompasses both positive and negative $P-E$ values compared to pre-industrial (ca. -2 to $+2$ mm/day; Figure 4), the lack of relationship between CO_2 and temperature in this zonally averaged view is perhaps unsurprising.

Our moisture budget analysis (Figure 8 and Figure S8 in Supporting Information S1) lends further insight into the mechanisms driving the simulated subtropical $P-E$ changes. Generally speaking, the time-mean component is the dominant component in the tropics, where the time-mean moisture transport typically dominates over the eddy component (Figures 8c and 8d). Changes in net $P-E$ values ($\delta(P-E)$) due to the time mean component can be further decomposed into: (a) changes in humidity assuming constant preindustrial circulation ($\bar{v}_{\text{cnt}} \delta \bar{q}$,

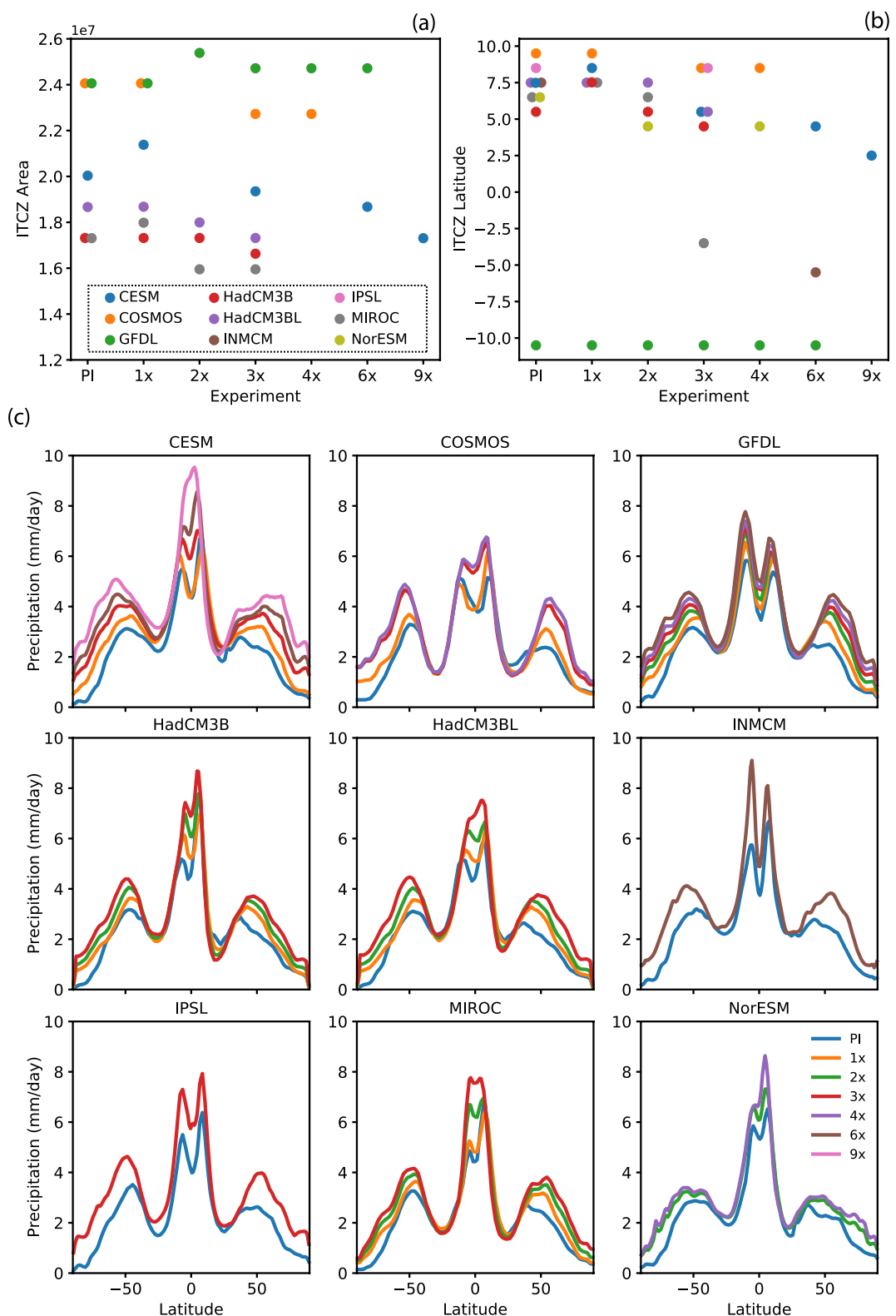


Figure 7. Zonal-mean mean annual precipitation (MAP) and Inter-Tropical Convergence Zone (ITCZ) characteristics in the Deep-Time Model Intercomparison Project (DeepMIP)-Eocene simulations. (a) The width of the ITCZ (defined as in Byrne and Schneider (2016)), (b) the ITCZ latitude of maximum precipitation and (c) the zonal-mean MAP profiles for each model.

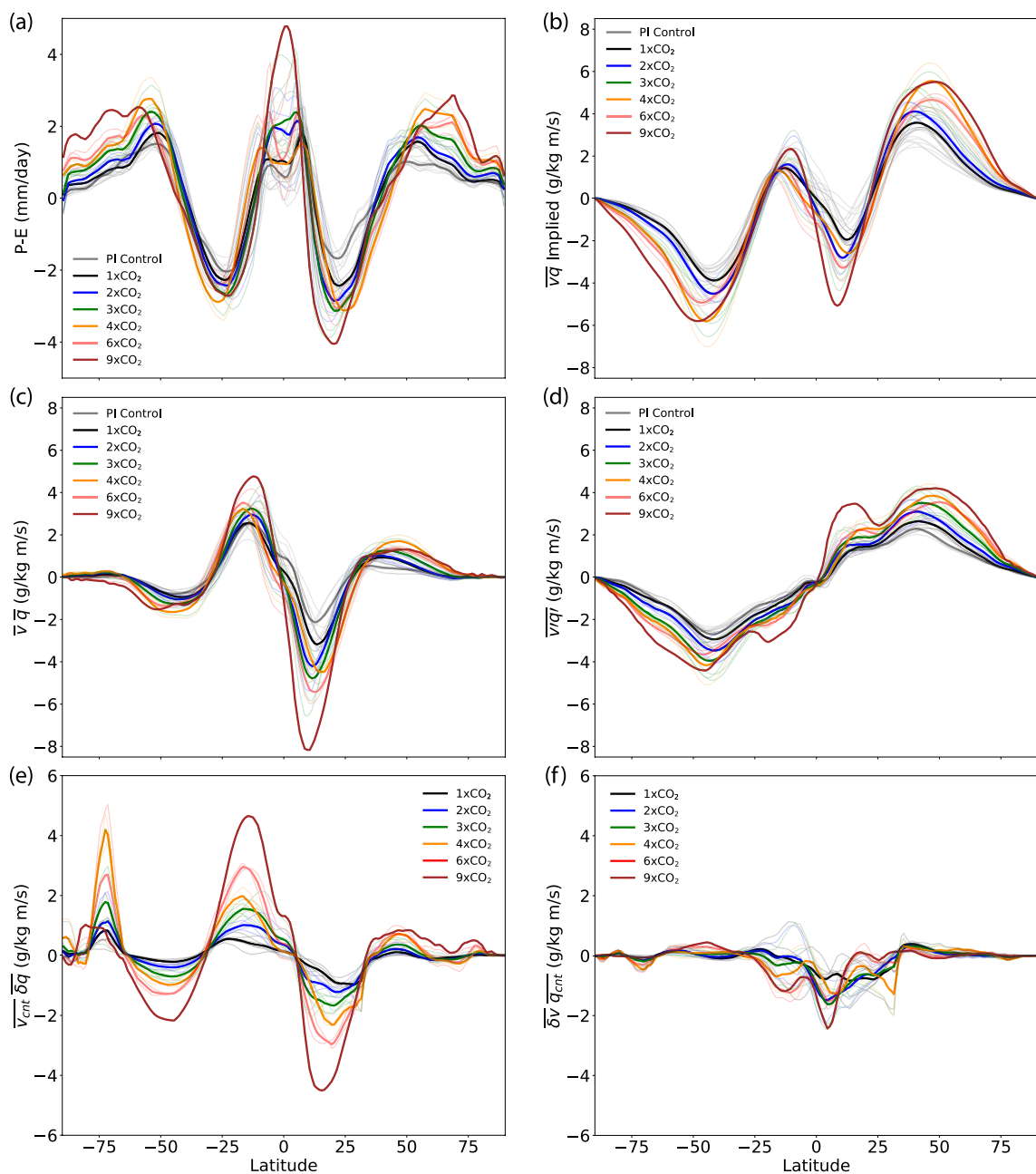


Figure 8. Zonal-mean components of the hydrological cycle as functions of latitude in the Deep-Time Model Intercomparison Project (DeepMIP) simulations. (a) surface precipitation minus evaporation ($P-E$), (b) implied moisture transport ($\bar{v}q$ implied in $\text{g}/\text{kg m/s}$), (c) moisture transport by time-mean flow ($\bar{v}\bar{q}$ in $\text{g}/\text{kg m/s}$), (d) moisture transport by eddy transport ($\bar{v}'\bar{q}'$ in $\text{g}/\text{kg m/s}$), (e) the contribution of changes in the time-mean humidity to changes in the time-mean moisture transport (i.e., thermodynamic effects) ($\bar{v}_{\text{cnt}}\delta\bar{q}$ in $\text{g}/\text{kg m/s}$), (f) the contribution of changes in the circulation to changes in time-mean moisture transport (i.e., dynamic effects) ($\delta\bar{v}\bar{q}_{\text{cnt}}$ in $\text{g}/\text{kg m/s}$). Full set of simulations is plotted as thin transparent colored lines, and the multi model mean as thick colored lines. Note that the MMM contains a different model ensemble for different CO_2 concentrations (see Figure 4 and Table S1 in Supporting Information S1). Note also that IPSL, INMCM, and NorESM are missing from the moisture budget analysis in this and subsequent plots because the atmospheric variables required were missing from the DeepMIP database.

the thermodynamic component of changes in the time mean moisture divergence), (b) changes in circulation assuming constant preindustrial humidity ($\delta\bar{v}\bar{q}_{\text{cnt}}$, the dynamic component of changes in the time mean moisture divergence), and (c) a perturbation term representing the coupling of changes in humidity and changes in circulation ($\delta\bar{v}\delta\bar{q}$) (Figures 8e and 8f and Figure S9 in Supporting Information S1):

$$\delta(P-E)_{\text{tm}} = -\nabla \cdot \frac{1}{g} \int_{p_t}^{p_s} v_{\text{cnt}} \delta q \, dp - \nabla \cdot \frac{1}{g} \int_{p_t}^{p_s} \delta v q_{\text{cnt}} \, dp - \nabla \cdot \frac{1}{g} \int_{p_t}^{p_s} \delta v \delta q \, dp + \text{RES}$$

where “tm” indicates time mean, δ represents the change in each variable between the study interval (i.e., the early Eocene) and the pre-industrial climate, and the residual term (RES) accounts for changes in the surface pressure bound of the integrals, which is dominated by topographic changes between the Eocene and pre-industrial experiments. With increasing temperatures, atmospheric humidity (q) is predicted to increase following the Clausius-Clapeyron relation. Assuming that the zonal-mean circulation (v) remains identical to pre-industrial ($\delta v = 0$), the dynamic term will be zero and the thermodynamic term will result in the tropics and high-latitudes becoming wetter (i.e., the moisture convergence into these regions in the control climate is enhanced) and the subtropics becoming drier (i.e., the moisture divergence from this region in the control climate is enhanced). Zonal-mean circulation changes are often considered secondary to changes in atmospheric humidity. However, it has been demonstrated that zonal-mean circulation changes may be important under certain climate scenarios (e.g., weak latitudinal temperature gradients) and may even compensate for changes in atmospheric humidity in regions such as the subtropics on zonal average (Burls & Fedorov, 2017). In a scenario where zonal-mean circulation (v)—specifically a decrease in Hadley cell strength—dominates over an increase in humidity (q), the subtropics on average will be characterized by reduced (rather than enhanced) moisture divergence and wetter (rather than drier) conditions (Burls & Fedorov, 2017).

Focusing on the subtropics in the DeepMIP simulations (Figure 9), higher GMST values indeed result in an increase in atmospheric humidity and enhanced subtropical moisture divergence. This leads to a corresponding decrease in $P-E$ (up to >-1.5 mm/day; Figure 9a) and is consistent with a “wet-gets-wetter, dry-gets-drier” scenario in warmer climates. However, this scenario is partially compensated by a reduction in LTGs, here taken as the difference between 15°S and 15°N and 30°–60°N/S. Reduced LTGs lead to a reduction in the strength of the zonal-mean subtropical circulation (v)—that is, the Hadley circulation—and a relative increase in subtropical zonal-mean $P-E$ (Figure 9b), particularly in the Southern Hemisphere where the strength of the Hadley Cell (Figure S10 in Supporting Information S1) systematically weakens with the LTG in all models (Figure 11e and Figure S12b in Supporting Information S1). The models differ more in the strength of the relationship between Hadley circulation changes and the LTG in the Northern Hemisphere (Figures S12d and S12f in Supporting Information S1), perhaps because of the complicating factor of inter-model differences in latitudinal ITCZ shift. The dynamical effect of weakened Hadley circulation is stronger in model simulations with weaker latitudinal temperature gradients (i.e., CESM and GFDL model simulations) and weaker in models with stronger latitudinal temperature gradients (e.g., HadCM3L) (Figure 9d and Figure S12b in Supporting Information S1). Therefore, the DeepMIP models with the lowest LTGs (e.g., CESM and GFDL) are characterized by higher subtropical MAP estimates relative to pre-industrial. Intriguingly, those models with reduced LTGs most closely reproduce temperature gradients (and GMST estimates) as reconstructed by proxies (Zhu et al., 2019; Figure 1 in Lunt et al., 2021). This implies that the early Eocene was likely characterized by a reduction in the strength of Hadley circulation. However, all DeepMIP models, including CESM and GFDL, show that the reduction in subtropical circulation (Figure 9d) is not sufficient to compensate fully for changes in atmospheric humidity (Figure 9c). As such, the subtropics are characterized by overall drier conditions in terms of $P-E$ in the DeepMIP ensemble (Figure 9a).

Extrapolating from this, if early Eocene LTGs were even weaker than suggested by these models (Lunt et al., 2021), Hadley circulation-induced changes may have outcompeted the thermodynamic changes, leading to overall wetter subtropics on zonal average (e.g., Burls & Fedorov, 2017). Although proxy-model bias has decreased over recent years for certain DeepMIP models, early Eocene proxy compilations still suggest weaker global equator-to-pole LTGs (~ 14 –22°C; Gaskell et al., 2022; Evans et al., 2018; Cramwinckel et al., 2018) than those predicted in the DeepMIP model ensemble (~ 18 –25°C; Figure 1b in Lunt et al., 2021). However, proxy-derived LTG estimates remain associated with large uncertainties due to proxy-inherent uncertainties, the use of different input datasets, and/or the analysis of different time intervals (*cf.* GMST estimates; Inglis et al., 2020). Taken together, this highlights the important role of accurately reconstructing and modeling the meridional temperature gradient when interpreting past meridional rainfall patterns.

3.4. Proxy-Based Precipitation Estimates During the Early Eocene

Our proxy synthesis indicates that high-latitude regions were characterized by high MAP estimates, consistent with previous results from the northern (Eberle & Greenwood, 2012; Salpin et al., 2019; Suan et al., 2017; West et al., 2015, 2020) and southern high-latitudes (Poole et al., 2005; Pross et al., 2012) (Figure 10). This is consistent with evidence for low-salinity sea surface conditions in the high northern latitudes near the termination of the EECO (~ 49 Ma) (i.e., the Azolla interval), although this salinity signal might be strongly linked to

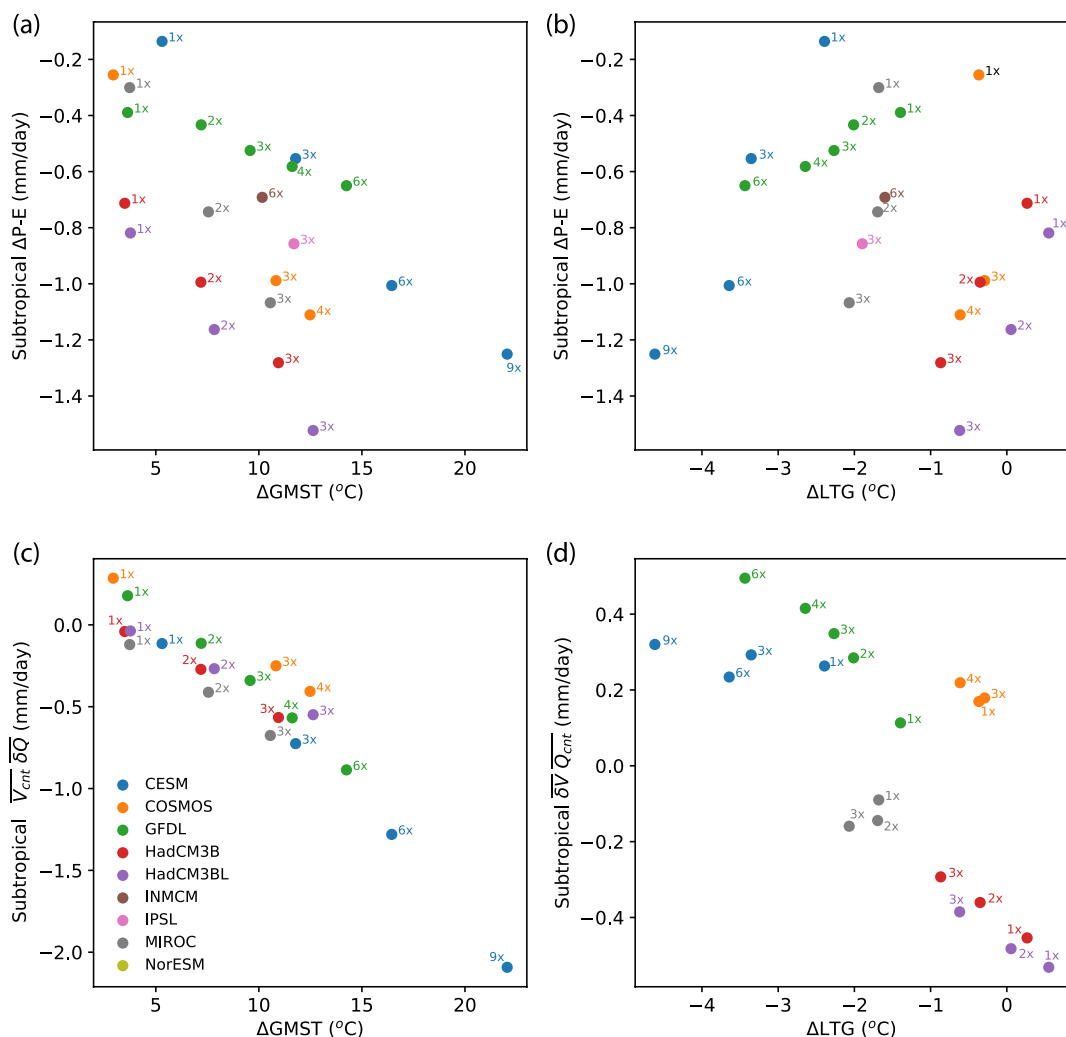


Figure 9. Subtropical moisture budget diagnostics show competing influence of atmospheric humidity and circulation in the subtropics (15° – 30° N/S). (a) the relationship between changes in subtropical precipitation-evaporation ($P-E$) and global mean surface temperature (GMST), (b) the relationship between changes in subtropical $P-E$ and the latitudinal temperature gradient (LTG) between 15° S and 15° N and 30° – 60° N/S, (c) changes in subtropical $P-E$ due to humidity-induced changes in the time-mean moisture transport divergence (i.e., thermodynamic effects), (d) changes in subtropical $P-E$ due to circulation-induced changes in the time-mean moisture transport divergence (i.e., dynamic effects).

paleogeographic change (Barke et al., 2012; Brinkhuis et al., 2006). Proxy estimates from more transient periods of warming (e.g., the PETM and Eocene Thermal Maximum 2; ETM2) provide additional support for high MAP in the Arctic (Pagani et al., 2006; Willard et al., 2019), the North Sea Basin (Collinson et al., 2003; Garel et al., 2013; Kender et al., 2012), and the southwest Pacific (Pancost et al., 2013; Sluijs et al., 2011). We note that in our compilation, early Eocene-aged CLAMP-derived MAP estimates from North America are much higher than most NLR estimates. CLAMP estimates are based on locally derived floral assemblages, whereas NLR estimates can reflect both locally derived floral elements but also floral elements transported over long distance (e.g., wind- or water-dispersed pollen). As a consequence, CLAMP estimates may reflect a bias toward wetter environments, whereas NLR estimates may be biased toward drier (upland) environments. The set of MAP estimates from Antarctica based on wood physiognomy are also far higher than the other proxies (Poole et al., 2005). Due to the lack of wood physiognomic MAP estimates from other regions, it is unclear whether these values are representative of the Antarctic continent.

Early Eocene tropical and subtropical MAP estimates are also relatively high (>2 – 4 mm/day, Figure 10). Although proxy-derived subtropical MAP values imply wetter conditions during the early Eocene, we note that these estimates are biased toward regions with well-preserved floral assemblages and, by extension, relatively

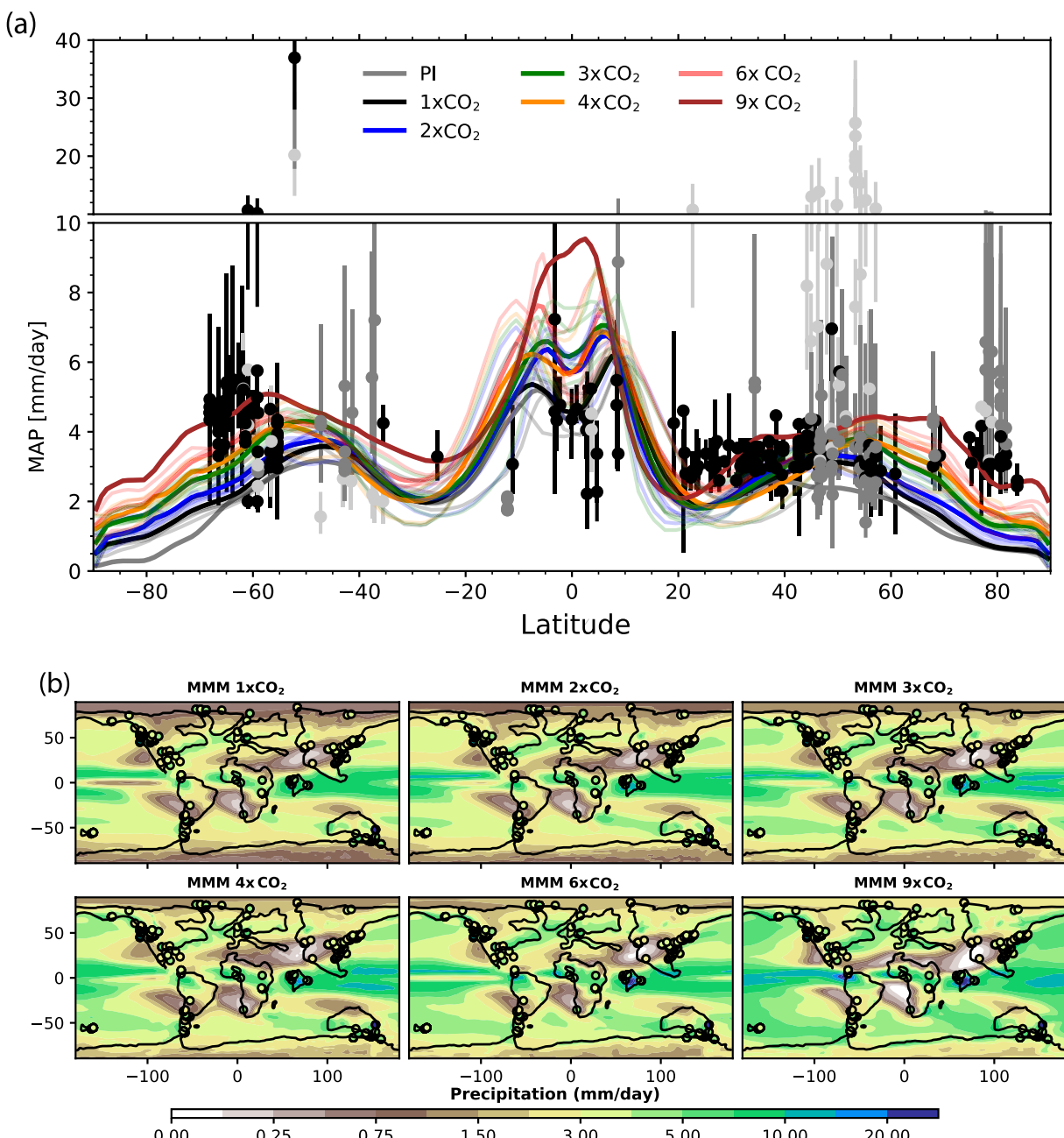


Figure 10. Proxy-based mean annual precipitation (MAP; mm/day) values overlaid on simulated MAP fields from the Deep-Time Model Intercomparison Project (DeepMIP) ensemble. (a) Zonal-mean MAP from all the DeepMIP-Eocene experiments (light colored lines) with the multi-model-mean as a bold line and the proxy estimate overlaid as symbols. See Figure S10 in Supporting Information S1 for individual model plots with simulated MAP values at the proxy locations rather than zonal-mean values. (b) MMM MAP for each DeepMIP-Eocene CO₂ experiment with the reconstructed MAP estimates overlaid.

wet regions. Subsequently, arid and semi-arid environments are likely under-sampled in our synthesis. Evidence from periods of superimposed warming during the Eocene suggests drier subtropics, with evidence for enhanced evapotranspiration in Tanzania during the onset of the PETM (Handley et al., 2012), drying in the continental interior (e.g., Bighorn Basin) during the body of the PETM (Kraus et al., 2013; Kraus & Riggins, 2007; Smith et al., 2007), and increased subtropical salinity in the central Pacific during ETM2 (Harper et al., 2017). Based on the sparsity of data for the early Eocene background state however, we cannot distinguish whether the lack of paleobotanical evidence for arid environments derives from sampling sparsity itself, from methodological bias, or from actual absence of such environments. Moving forward, we suggest that alternative proxies, for example,

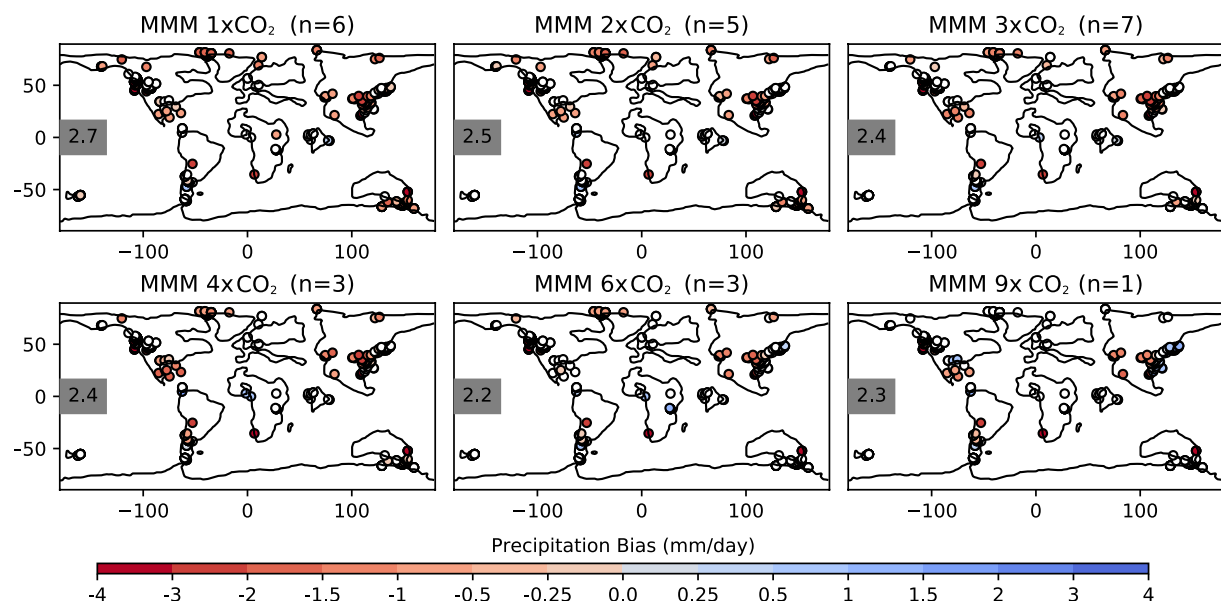


Figure 11. Data-model comparison for the early Eocene. In each panel, the early Eocene multi-model-mean (MMM) mean annual precipitation (MAP) bias is shown for a given CO_2 concentration. The root-mean-square error of the bias across all the sites is shown in black on the left. Lower values indicate a closer data-model agreement.

clumped isotope- $\delta^{18}\text{O}$ analysis of pedogenic siderites (van Dijk et al., 2020), could help to reconstruct hydrological change in arid and semi-arid environments where plant macrofossils are unlikely to be preserved, and the availability of plant-based terrestrial proxy data will therefore be limited or absent. These caveats will need to be addressed in the future to fully establish the fidelity with which the DeepMIP-Eocene models simulate the tropical and subtropical hydrological cycle response over land. In this study, we proceed by evaluating the models with our synthesis of paleobotanical MAP estimates.

3.5. Terrestrial Precipitation Data-Model Comparison

To explore whether the DeepMIP models realistically reproduce regional MAP patterns during the early Eocene, we employ the data-model comparison approach outlined in Section 2.2.3 using our new and published botanical-based MAP estimates. Although the “wet-gets-wetter, dry-gets-drier” response may not hold true over land (Byrne & O’Gorman, 2015), our terrestrial data-model comparison helps us assess overall model performance. A previous site-by-site data-model comparison (Carmichael et al., 2016) suggested that the EoMIP models were able to reproduce key features of the hydrological cycle in the mid-latitudes (e.g., western US interior, central Europe), but modeled MAP estimates were typically lower than those from proxies in the high-latitudes (e.g., East Antarctica, SE Australia, Axel Heiberg). For the new DeepMIP-Eocene model-data comparison, we find a similar result (Figures 11 and 12). The MMM underestimates proxy-derived MAP in the high northern latitudes, especially at lower CO_2 levels (Figure 11). We attribute this mismatch to the lack of polar amplification in certain models, especially at lower CO_2 levels (e.g., HadCM3, COSMOS) (Lunt et al., 2021, Figure S11 in Supporting Information S1). At high CO_2 values, the model-data bias for high-latitude MAP is smallest, down to -0.4 to -0.6 mm/day for the $6\times$ and $9\times\text{CO}_2$ simulations (Figure 12d). The mid latitudes are likewise associated with large data-model mismatches, with models simulating MAP values that are too low by ~ 0.4 – 1.3 mm/day from a zonal-mean perspective, and a decrease in bias with increasing CO_2 levels (Figure 12c). Moving to the subtropics, model-bias is likewise negative, with a large range between near-zero and -1.75 , but without a clear intra- or inter-model improvement with CO_2 levels. Finally, almost all models (expect for COSMOS) simulate too much precipitation in the tropics compared to the reconstructions, with positive biases of up to $+1.5$ mm/day, that remain similar or worsen with increasing CO_2 for a given model (Figure 12a).

Comparing between models, proxy-model mismatches are lowest for CESM, GFDL, MIROC and NorESM in the subtropics, mid- and high latitudes (Figure 12; Figure S11 in Supporting Information S1) that is, the models with higher GMST estimates and lower LTGs (Lunt et al., 2021). These models overall simulate higher precipitation.

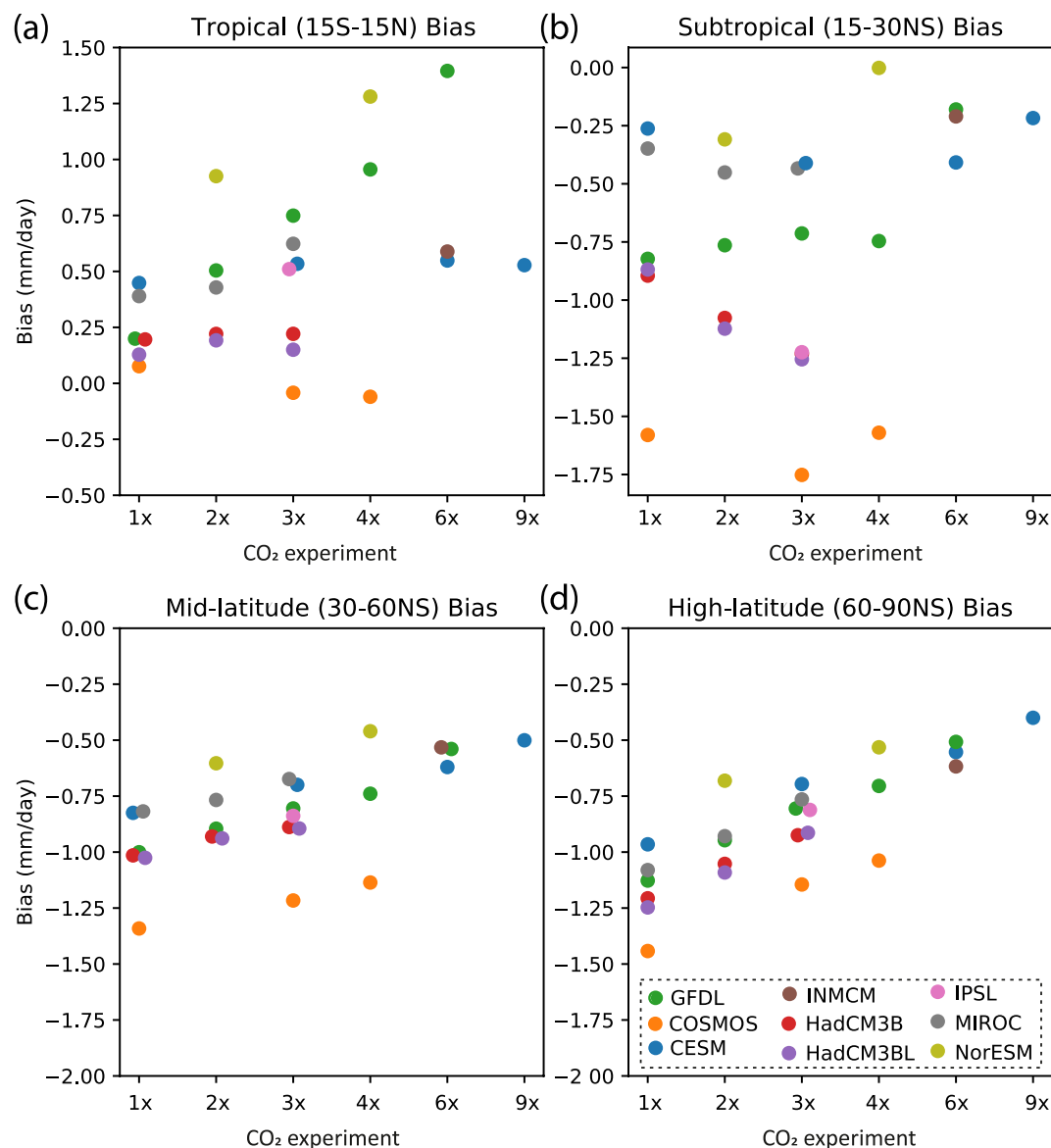


Figure 12. Zonally averaged model-data mean annual precipitation (MAP) bias for the (a) tropics (15° – 15° N/S), (b) subtropics (15° – 30° N/S), (c) mid latitudes (30° – 60° N/S), and (d) high latitudes (60° – 90° N/S). Panels (a–d) show the model-data bias in mm/day for the different model simulations, sorted by CO₂ forcing.

They however do not outperform the other models in the tropical band (Figure 12a). From a regional viewpoint, in the mid-latitudes the MMM either underestimates MAP (e.g., western South America and Tibet) or overestimates MAP (e.g., western North America; Figure 11). As these mismatches lie close to major mountain ranges (e.g., Rocky Mountains, proto-Tibetan Plateau, Andes), it is possible that mismatches are due to topographic effects as a small offset in reconstructed paleolocation can make a large difference in reconstructed elevation. Additionally, the DeepMIP Eocene model resolution is coarse and the topography has inherent uncertainty, especially in the North American Cordillera and proto-Himalayas (Herold et al., 2014). In our MMM comparison, it should be noted that the composition of the model ensemble changes over the different CO₂ levels in the MMM (cf. Table S1 in Supporting Information S1 and Figure 4). For instance, whereas the 3xCO₂ experiment was performed with 7 out of 8 DeepMIP models, only 3 models (CESM, GFDL, INMCM) were used for the 6x CO₂ experiment, and only CESM ran a 9xCO₂ simulation. For a more detailed analysis of regional hydroclimate in the DeepMIP simulations, we refer the reader to Williams et al. (2022) and Reichgelt et al. (2022), for the African and Australian continent, respectively.

In summary, our results indicate that the models with higher GMST and weaker LTGs are able to better simulate the global and regional scale hydrological cycle (Figure 12). Overall, our integrated data-model approach suggests that the early Eocene was characterized by a thermodynamically dominated hydrological response to warming within the mid and high latitudes. Enhanced polar amplified warming in response to increased CO₂ forcing leads to an improved high-latitude model-proxy fit with enhanced local evaporation and eddy moisture transport convergence increasing precipitation (Figures 12c and 12d; Figures S6 and S11 in Supporting Information S1). Furthermore, the DeepMIP-Eocene models on average simulate higher precipitation in the tropics relative to the proxy data (Figure 12a and Figure S11 in Supporting Information S1), with increased tropical precipitation driven by enhanced local evaporation and time-mean moisture convergence. While several DeepMIP-Eocene models simulate a narrowing of the ITCZ, an ITCZ narrowing signal is not clearly evident within the proxy data (Figure 10). Lastly, in the subtropical latitudes, the models differ widely in their response leading to varying degrees of model-data bias (Figure 12b). Weakened Hadley circulation in response to weaker LTGs could have offset thermodynamic subtropical drying and supported regional wetting, as seen to some extent in the GFDL and CESM models (Figure 12b and Figure S10 in Supporting Information S1). Although the lack of proxy evidence for arid subtropical regions in the early Eocene background state might be caused by a bias of the sparsely available data to wet regions, this conspicuous absence of evidence at least suggests regionally wetter conditions.

4. Conclusions

Here we use the DeepMIP model simulations to investigate global and zonal mean rainfall patterns during the early Eocene (~56.0–47.8 million years ago). Across the DeepMIP ensemble, higher GMST estimates are associated with higher global mean MAP estimates, with an overall 2.4% increase in global MAP per degree of warming. At higher temperatures, the DeepMIP model simulations indicate that - on average - the low- (0°–15°N/S) and high-latitudes (>60°N/S) are characterized by positive *P*–*E* values (wetter conditions). While the subtropics (15°–30°N/S) are characterized by negative *P*–*E* values (drier conditions), there is large inter-model variability in subtropical MAP due to the competing influence of humidity (i.e., thermodynamic changes) and atmospheric circulation (i.e., dynamic changes) in this region. Overall, the DeepMIP models underestimate MAP estimates in the subtropics and mid-to-high latitudes and overestimate MAP in the deep tropics. The DeepMIP model simulations that exhibit higher subtropical MAP estimates relative to pre-industrial are characterized by weaker latitudinal temperature gradients and a reduction in subtropical moisture divergence. This acts to offset drier conditions, particularly in the Southern Hemisphere where the strength of the Hadley Cell systematically weakens with the latitudinal temperature gradient in all models. Crucially, the models with reduced latitudinal temperature gradients (e.g., GFDL, CESM) more closely reproduce our compilation of proxy-derived precipitation estimates and other key climate metrics. Taken together, this implies weaker subtropical circulation in the early Eocene. However, changes in subtropical moisture divergence were not sufficient to induce subtropical wetting in the models. Extrapolating from this, if early Eocene latitudinal temperature gradients were even weaker than suggested by these models, circulation-induced changes may have outcompeted the thermodynamic changes, leading to overall wetter subtropics—consistent with sparsely available proxy data. Taken together, our study highlights the importance of accurately reconstructing and modeling the meridional temperature gradient when interpreting past subtropical rainfall patterns.

Conflict of Interest

The authors declare no conflicts of interest relevant to this study.

Data Availability Statement

The paleobotanical data used to calculate mean annual precipitation (MAP) estimates is available at OSF and associated with a CC-BY 4.0 license (Cramwinckel, 2023). Version 1.0.0 of the DeepMIP-Eocene model database used to simulate Eocene climate is preserved online (<https://www.deepmip.org/data-eocene>) and openly available via the University of Bristol Research Data Storage Facility (RDSF) (Lunt, 2023).

Acknowledgments

G.N.I was supported by a Royal Society Dorothy Hodgkin Fellowship (DHF/R1191178). G.N.I. was also supported by additional funds from the Royal Society (DHF/ERE/210068). N.J.B. was supported by the National Science Foundation, via award AGS-1844380. D. G was supported by the Natural Sciences and Engineering Research Council of Canada (NSERC) through Discovery Grants (DG 311934 and 2016-04337). C.K.W acknowledges funding from a private donor to the Northern Climates Postdoctoral Fellowship at the University of Alberta. D.K.H acknowledges support from Australian Research Council grant DE22010079 and the Australian Centre for Excellence in Antarctic Science, project number SR200100008. R.F is supported by NSF-2114204. A.dB was supported by Swedish Research Council project 2020-04791. The GFDL simulations were performed by resources provided by the Swedish National Infrastructure for Computing (SNIC) at the National Supercomputer Centre (NSC), partially funded by the Swedish Research Council through Grant agreement 2018-05973. W.L.C and A.A.O acknowledge funding from JSPS KAKENHI (Grant 17H06104) and MEXT KAKENHI (Grant 17H06323). The CESM project is supported primarily by the National Science Foundation (NSF); this material is based upon work supported by the National Center for Atmospheric Research, which is a major facility sponsored by the NSF under Cooperative Agreement 1852977.

References

Adeonipekun, P. A., Ehinola, O. A., Toluhi, Y., Toluhi, I. A., & Oyelami, A. (2012). Bio-sequence stratigraphy of Shagamu Quarry Outcrop. *Benin Basin, Southwestern Nigeria*.

Aleksandrova, G. N., Kodrul, T. M., & Jin, J. H. (2015). Palynological and paleobotanical investigations of Paleogene sections in the Maoming basin, South China. *Stratigraphy and Geological Correlation*, 23(3), 300–325. <https://doi.org/10.1134/S0869593815030028>

Anagnostou, E., John, E. H., Babilia, T. L., Sexton, P. F., Ridgwell, A., Lunt, D. J., et al. (2020). Proxy evidence for state-dependence of climate sensitivity in the Eocene greenhouse. *Nature Communications*, 11(1), 4436. <https://doi.org/10.1038/s41467-020-17887-x>

Barke, J., van der Burgh, J., van Konijnenburg-Cittert, J. H. A., Collinson, M. E., Pearce, M. A., Bujak, J., et al. (2012). Coeval Eocene blooms of the freshwater fern Azolla in and around Arctic and Nordic seas. *Palaeogeography, Palaeoclimatology, Palaeoecology*, 337–338, 108–119. <https://doi.org/10.1016/j.palaeo.2012.04.002>

Bhattacharya, T., Feng, R., Tierney, J. E., Rubelke, C., Burls, N., Knapp, S., & Fu, M. (2022). Expansion and intensification of the North American monsoon during the Pliocene. *AGU Advances*, 3(6), e2022AV000757. <https://doi.org/10.1029/2022AV000757>

Brinkhuis, H., Schouten, S., Collinson, M. E., Sluijs, A., Damsté, J. S. S., Dickens, G. R., et al. (2006). Episodic fresh surface waters in the Eocene Arctic Ocean. *Nature*, 441(7093), 606–609. <https://doi.org/10.1038/nature04692>

Burls, N. J., Bradshaw, C. D., Boer, A. M. D., Herold, N., Huber, M., Pound, M., et al. (2021). Simulating Miocene warmth: Insights from an opportunistic multi-model ensemble (MioMIP1). *Paleoceanography and Paleoclimatology*, 36, e2020PA004054. <https://doi.org/10.1029/2020PA004054>

Burls, N. J., & Fedorov, A. V. (2017). Wetter subtropics in a warmer world: Contrasting past and future hydrological cycles. *Proceedings of the National Academy of Sciences*, 114(49), 12888–12893. <https://doi.org/10.1073/pnas.1703421114>

Byrne, M. P., & O’Gorman, P. A. (2015). The response of precipitation minus evapotranspiration to climate warming: Why the “wet-get-wetter, dry-get-drier” scaling does not hold over land. *Journal of Climate*, 28(20), 8078–8092. <https://doi.org/10.1175/JCLI-D-15-0369.1>

Byrne, M. P., & Schneider, T. (2016). Energetic constraints on the width of the intertropical convergence zone. *Journal of Climate*, 29(13), 4709–4721. <https://doi.org/10.1175/JCLI-D-15-0767.1>

Cantrill, D. J., Bamford, M. K., Wagstaff, B. E., & Sauquet, H. (2013). Early Eocene fossil plants from the Mwadui kimberlite pipe, Tanzania. *Review of Palaeobotany and Palynology*, 196, 19–35. <https://doi.org/10.1016/j.revpalbo.2013.04.002>

Carmichael, M. J., Inglis, G. N., Badger, M. P. S., Naafs, B. D. A., Behrooz, L., Remmeltzaal, S., et al. (2017). Hydrological and associated biogeochemical consequences of rapid global warming during the Paleocene-Eocene thermal maximum. *Global and Planetary Change*, 157, 114–138. <https://doi.org/10.1016/j.gloplacha.2017.07.014>

Carmichael, M. J., Lunt, D. J., Huber, M., Heinemann, M., Kiehl, J., LeGrande, A., et al. (2016). A model–model and data–model comparison for the early Eocene hydrological cycle. *Climate of the Past*, 12(2), 455–481. <https://doi.org/10.5194/cp-12-455-2016>

Carrapa, B., Clementz, M., & Feng, R. (2019). Ecological and hydroclimate responses to strengthening of the Hadley circulation in South America during the Late Miocene cooling. *Proceedings of the National Academy of Sciences*, 116(20), 9747–9752. <https://doi.org/10.1073/pnas.1810721116>

Collinson, M. E., Hooker, J. J., & Groecke, D. R. (2003). Cobham lignite bed and penecontemporaneous macrofloras of southern England: A record of vegetation and fire across the Paleocene-Eocene thermal maximum. <https://doi.org/10.1130/0-8137-2369-8.333>

Cramwinckel, M. J. (2023). Global and zonal-mean hydrological response to early Eocene warmth. [Dataset]. <https://doi.org/10.17605/OSF.IO/M7B4K>

Cramwinckel, M. J., Huber, M., Kocken, I. J., Agnini, C., Bijl, P. K., Bohaty, S. M., et al. (2018). Synchronous tropical and polar temperature evolution in the Eocene. *Nature*, 559(7714), 382–386. <https://doi.org/10.1038/s41586-018-0272-2>

Eberle, J. J., & Greenwood, D. R. (2012). Life at the top of the greenhouse Eocene world—A review of the Eocene flora and vertebrate fauna from Canada’s High Arctic. *Geological Society of America Bulletin*, 124, 3–23. <https://doi.org/10.1130/B30571.1>

Eisawi, A., & Schrank, E. (2008). Upper Cretaceous to Neogene palynology of the Melut Basin, Southeast Sudan. *Palynology*, 32(1), 101–129. <https://doi.org/10.1080/01916122.2008.9989653>

Evans, D., Sagoo, N., Renema, W., Cotton, L. J., Müller, W., Todd, J. A., et al. (2018). Eocene greenhouse climate revealed by coupled clumped isotope-Mg/Ca thermometry. *Proceedings of the National Academy of Sciences of the United States of America*, 201714744. <https://doi.org/10.1073/pnas.1714744115>

Eyring, V., Bony, S., Meehl, G. A., Senior, C. A., Stevens, B., Stouffer, R. J., & Taylor, K. E. (2016). Overview of the Coupled Model Inter-comparison Project Phase 6 (CMIP6) experimental design and organization. *Geoscientific Model Development*, 9(5), 1937–1958. <https://doi.org/10.5194/gmd-9-1937-2016>

Fauquette, S., Guiot, J., & Suc, J.-P. (1998). A method for climatic reconstruction of the Mediterranean Pliocene using pollen data. *Palaeogeography, Palaeoclimatology, Palaeoecology*, 144(1–2), 183–201. [https://doi.org/10.1016/S0031-0182\(98\)00083-2](https://doi.org/10.1016/S0031-0182(98)00083-2)

Feng, R., Bhattacharya, T., Otto-Bliesner, B. L., Brady, E. C., Haywood, A. M., Tindall, J. C., et al. (2022). Past terrestrial hydroclimate sensitivity controlled by Earth system feedbacks. *Nature Communications*, 13(1), 1306. <https://doi.org/10.1038/s41467-022-28814-7>

Frederiksen, N. (1994). Middle and late Paleocene angiosperm pollen from Pakistan. *Palynology*, 18(1), 91–137. <https://doi.org/10.1080/01916122.1994.9989442>

Garel, S., Schnyder, J., Jacob, J., Dupuis, C., Boussafir, M., Le Milbeau, C., et al. (2013). Paleohydrological and paleoenvironmental changes recorded in terrestrial sediments of the Paleocene–Eocene boundary (Normandy, France). *Palaeogeography, Palaeoclimatology, Palaeoecology*, 376, 184–199. <https://doi.org/10.1016/j.palaeo.2013.02.035>

Gaskell, D. E., Huber, M., O’Brien, C. L., Inglis, G. N., Acosta, R. P., Poulsen, C. J., & Hull, P. M. (2022). The latitudinal temperature gradient and its climate dependence as inferred from foraminiferal 8180 over the past 95 million years. *Proceedings of the National Academy of Sciences*, 119(11), e2111332119. <https://doi.org/10.1073/pnas.2111332119>

Givnish, T. J. (1984). Leaf and canopy adaptations in tropical forests. In E. Medina, H. A. Mooney, & C. Vázquez-Yáñez (Eds.), *Physiological ecology of plants in the wet tropics*, (Vol. 12, pp. 51–84). Springer Netherlands. https://doi.org/10.1007/978-94-009-7299-5_6

Graham, A., Cozadd, D., Areces-Mallea, A., & Frederiksen, N. O. (2000). Studies in Neotropical paleobotany. XIV. A palynoflora from the middle Eocene Saramaguacán Formation of Cuba. *American Journal of Botany*, 87(10), 1526–1539. <https://doi.org/10.2307/2656879>

Greenwood, D. R. (2007). Fossil angiosperm leaves and climate: From Wolfe and Dilcher to Burnham and Wilf. *Courier Forschungsinstitut Senckenberg*, 258, 95–108.

Greenwood, D. R., Moss, P. T., Rowett, A. I., Vadala, A. J., & Keefe, R. L. (2003). Plant communities and climate change in southeastern Australia during the early Paleogene. In S. L. Wing, P. D. Gingerich, B. Schmitz, & E. Thomas (Eds.), *Causes and consequences of globally warm climates in the early Paleogene* (pp. 365–380). Geological Society of America.

Hailemichael, M., Aronson, J. L., Savin, S., Tevesz, M. J. S., & Carter, J. G. (2002). δ₁₈O in mollusk shells from Pliocene Lake Hadar and modern Ethiopian lakes: Implications for history of the Ethiopian monsoon. *Palaeogeography, Palaeoclimatology, Palaeoecology*, 186(1–2), 81–99. [https://doi.org/10.1016/S0031-0182\(02\)00445-5](https://doi.org/10.1016/S0031-0182(02)00445-5)

Handley, L., O'Halloran, A., Pearson, P. N., Hawkins, E., Nicholas, C. J., Schouten, S., et al. (2012). Changes in the hydrological cycle in tropical East Africa during the Paleocene–Eocene thermal maximum. *Palaeogeography, Palaeoclimatology, Palaeoecology*, 329–330, 10–21. <https://doi.org/10.1016/j.palaeo.2012.02.002>

Harper, D. T., Zeebe, R., Hönisch, B., Schrader, C. D., Lourens, L. J., & Zachos, J. C. (2017). Subtropical sea-surface warming and increased salinity during Eocene Thermal Maximum 2. *Geology*, 46, 187–190. <https://doi.org/10.1130/G39658.1>

Held, I. M., & Soden, B. J. (2006). Robust responses of the hydrological cycle to global warming. *Journal of Climate*, 19(21), 5686–5699. <https://doi.org/10.1175/JCLI3990.1>

Herman, A. B., Spicer, R. A., Aleksandrova, G. N., Yang, J., Kodrul, T. M., Maslova, N. P., et al. (2017). Eocene–early Oligocene climate and vegetation change in southern China: Evidence from the Maoming Basin. *Palaeogeography, Palaeoclimatology, Palaeoecology*, 479, 126–137. <https://doi.org/10.1016/j.palaeo.2017.04.023>

Herold, N., Buzan, J., Seton, M., Goldner, A., Green, J. A. M., Müller, R. D., et al. (2014). A suite of early Eocene (~55 Ma) climate model boundary conditions. *Geoscientific Model Development*, 7(5), 2077–2090. <https://doi.org/10.5194/gmd-7-2077-2014>

Hijmans, R. J., Phillips, S., Leathwick, J., & Elith, J. (2020). dismo: Species distribution modeling.

Hoegh-Guldberg, O., Jacob, D., Taylor, M., Bindu, M., Brown, S., Camilloni, I., et al. (2018). Impacts of 1.5°C global warming on natural and human systems. In V. Masson-Delmotte, P. Zhai, H.-O. Pörtner, D. Roberts, J. Skea, P. R. Shukla, et al. (Eds.), *Global Warming of 1.5°C. An IPCC Special Report on the impacts of global warming of 1.5°C above pre-industrial levels and related global greenhouse gas emission pathways, in the context of strengthening the global response to the threat of climate change, sustainable development, and efforts to eradicate poverty*.

Hollis, C. J., Dunkley Jones, T., Anagnostou, E., Bijl, P. K., Cramwinckel, M. J., Cui, Y., et al. (2019). The DeepMIP contribution to PMIP4: Methodologies for selection, compilation and analysis of latest Paleocene and early Eocene climate proxy data, incorporating version 0.1 of the DeepMIP database. *Geoscientific Model Development*, 12(7), 3149–3206. <https://doi.org/10.5194/gmd-12-3149-2019>

Inglis, G. N., Bragg, F., Burls, N. J., Cramwinckel, M. J., Evans, D., Foster, G. L., et al. (2020). Global mean surface temperature and climate sensitivity of the early Eocene Climatic Optimum (EECO), Paleocene–Eocene thermal maximum (PETM), and latest Paleocene. *Climate of the Past*, 16(5), 1953–1968. <https://doi.org/10.5194/cp-16-1953-2020>

Jaramillo, C. A., Bayona, G., Pardo-Trujillo, A., Rueda, M., Torres, V., Harrington, G. J., & Mora, G. (2007). The palynology of the Cerrejón Formation (upper Paleocene) of northern Colombia. *Palynology*, 31(1), 153–189. <https://doi.org/10.2113/gspalynol.31.1.153>

Jarzen, D. M., & Klug, C. (2010). A preliminary investigation of a lower to middle Eocene palynoflora from Pine Island, Florida, USA. *Palynology*, 34(2), 164–179. <https://doi.org/10.1080/01916121003737421>

Kageyama, M., Braconnot, P., Harrison, S. P., Haywood, A. M., Jungclaus, J. H., Otto-Bliesner, B. L., et al. (2018). The PMIP4 contribution to CMIP6–Part 1: Overview and over-arching analysis plan. *Geoscientific Model Development*, 11(3), 1033–1057. <https://doi.org/10.5194/gmd-11-1033-2018>

Kender, S., Stephenson, M. H., Riding, J. B., Leng, M. J., Knox, R. W. O., Peck, V. L., et al. (2012). Marine and terrestrial environmental changes in NW Europe preceding carbon release at the Paleocene–Eocene transition. *Earth and Planetary Science Letters*, 353–354, 108–120. <https://doi.org/10.1016/j.epsl.2012.08.011>

Kennedy, E. M., Arens, N. C., Reichgelt, T., Spicer, R. A., Spicer, T. E. V., Stranks, L., & Yang, J. (2014). Deriving temperature estimates from Southern Hemisphere leaves. *Palaeogeography, Palaeoclimatology, Palaeoecology*, 412, 80–90. <https://doi.org/10.1016/j.palaeo.2014.07.015>

Kraus, M. J., McInerney, F. A., Wing, S. L., Secord, R., Baczyński, A. A., & Bloch, J. I. (2013). Paleohydrologic response to continental warming during the Paleocene–Eocene thermal maximum, Bighorn Basin, Wyoming. *Palaeogeography, Palaeoclimatology, Palaeoecology*, 370, 196–208. <https://doi.org/10.1016/j.palaeo.2012.12.008>

Kraus, M. J., & Riggins, S. (2007). Transient drying during the Paleocene–Eocene thermal maximum (PETM): Analysis of paleosols in the Bighorn Basin, Wyoming. *Palaeogeography, Palaeoclimatology, Palaeoecology*, 245(3–4), 444–461. <https://doi.org/10.1016/j.palaeo.2006.09.011>

Lunt, D. J. (2023). The DeepMIP model database (version 1.0). [Dataset]. University of Bristol Research Data Storage Facility (RDSF). <https://www.deepmip.org/data-eocene/>

Lunt, D. J., Bragg, F., Chan, W. L., Hutchinson, D. K., Ladant, J. B., Morozova, P., et al. (2021). DeepMIP: Model intercomparison of early Eocene climatic optimum (EECO) large-scale climate features and comparison with proxy data. *Climate of the Past*, 17(1), 203–227. <https://doi.org/10.5194/cp-17-203-2021>

Lunt, D. J., Bragg, F., Chan, W. L., Hutchinson, D. K., Ladant, J. B., Niezgodzki, I., et al. (2020). DeepMIP: Model intercomparison of early Eocene climatic optimum (EECO) large-scale climate features and comparison with proxy data. *Climate of the Past Discussions*, 1–27.

Lunt, D. J., Huber, M., Anagnostou, E., Baatsen, M. L., Caballero, R., DeConto, R., et al. (2017). The DeepMIP contribution to PMIP4: Experimental design for model simulations of the EECO, PETM, and pre-PETM (version 1.0). *Geoscientific Model Development*, 10(2), 889–901.

Masson-Delmotte, V., Zhai, P., Pirani, A., Connors, S. L., Péan, C., Chen, Y., et al. (2022). IPCC, 2021: Climate change 2021: The physical science basis. *Contribution of Working Group I to the Sixth Assessment Report of the Intergovernmental Panel on Climate Change*. Cambridge University Press.

Matthews, K. J., Maloney, K. T., Zahirovic, S., Williams, S. E., Seton, M., & Mueller, R. D. (2016). Global plate boundary evolution and kinematics since the late Paleozoic. *Global and Planetary Change*, 146, 226–250. <https://doi.org/10.1016/j.gloplacha.2016.10.002>

Mosbrugger, V., & Utescher, T. (1997). The coexistence approach—A method for quantitative reconstructions of tertiary terrestrial palaeoclimate data using plant fossils. *Palaeogeography, Palaeoclimatology, Palaeoecology*, 134(1–4), 61–86. [https://doi.org/10.1016/S0031-0182\(96\)00154-X](https://doi.org/10.1016/S0031-0182(96)00154-X)

Müller, R. D., Qin, X., Sandwell, D. T., Dutkiewicz, A., Williams, S. E., Flament, N., et al. (2016). The GPlates portal: Cloud-based interactive 3D visualization of global geophysical and geological data in a web browser. *PLoS One*, 11(3), e0150883. <https://doi.org/10.1371/journal.pone.0150883>

Pagani, M., Pedentchouk, N., Huber, M., Sluijs, A., Schouten, S., Brinkhuis, H., et al. (2006). Arctic hydrology during global warming at the Palaeocene/Eocene thermal maximum. *Nature*, 442(7103), 671–675. <https://doi.org/10.1038/nature05043>

Pancost, R. D., Taylor, K. W. R., Inglis, G. N., Kennedy, E. M., Handley, L., Hollis, C. J., et al. (2013). Early Paleogene evolution of terrestrial climate in the SW Pacific, Southern New Zealand. *Geochemistry, Geophysics, Geosystems*, 14(12), 5413–5429. <https://doi.org/10.1002/2013GC004935>

Pardo-Trujillo, A., Jaramillo, C. A., & Oboho-Ikuenobe, F. E. (2003). Paleogene palynostratigraphy of the eastern middle Magdalena Valley, Colombia. *Palynology*, 27(1), 155–178. <https://doi.org/10.1080/01916122.2003.9989585>

Pendergrass, A. G. (2020). The global-mean precipitation response to CO₂-induced warming in CMIP6 models. *Geophysical Research Letters*, 47(17), e2020GL089964. <https://doi.org/10.1029/2020GL089964>

Peppe, D. J., Royer, D. L., Cariglino, B., Oliver, S. Y., Newman, S., Leigh, E., et al. (2011). Sensitivity of leaf size and shape to climate: Global patterns and paleoclimatic applications. *New Phytologist*, 190(3), 724–739. <https://doi.org/10.1111/j.1469-8137.2010.03615.x>

Poole, I., & Bergen, P. F. (2006). Physiognomic and chemical characters in wood as palaeoclimate proxies. In J. Rozema, R. Aerts, & H. Cornelissen (Eds.), *Plants and climate change* (pp. 175–196). Springer Netherlands. https://doi.org/10.1007/978-1-4020-4443-4_12

Poole, I., Cantrill, D., & Utescher, T. (2005). A multi-proxy approach to determine Antarctic terrestrial palaeoclimate during the Late Cretaceous and Early Tertiary. *Palaeogeography, Palaeoclimatology, Palaeoecology*, 222(1–2), 95–121. <https://doi.org/10.1016/j.palaeo.2005.03.011>

Pross, J., Contreras, L., Bijl, P. K., Greenwood, D. R., Bohaty, S. M., Schouten, S., et al. (2012). Persistent near-tropical warmth on the Antarctic continent during the early Eocene epoch. *Nature*, 488(7409), 73–77. <https://doi.org/10.1038/nature11300>

Pross, J., Klotz, S., & Mosbrugger, V. (2000). Reconstructing palaeotemperatures for the Early and Middle Pleistocene using the mutual climatic range method based on plant fossils. *Quaternary Science Reviews*, 19(17–18), 1785–1799. [https://doi.org/10.1016/S0277-3791\(00\)00089-5](https://doi.org/10.1016/S0277-3791(00)00089-5)

Quattrochi, M. E., & Volkheimer, W. (2000). Paleoclimatic changes during the Paleocene-lower Eocene in the Salta Group Basin, NW Argentina. In P. Smolka, & W. Volkheimer (Eds.), *Southern Hemisphere paleo- and neoclimates: Key sites, methods, data and models* (pp. 353–367). Springer. https://doi.org/10.1007/978-3-642-59694-0_22

Reichgelt, T., Greenwood, D. R., Steinig, S., Conran, J. G., Hutchinson, D. K., Lunt, D. J., et al. (2022). Plant proxy Evidence for high rainfall and productivity in the Eocene of Australia. *Palaeogeography, Palaeoclimatology, Palaeoecology*, 37, e2022PA004418. <https://doi.org/10.1029/2022PA004418>

Reichgelt, T., Kennedy, E. M., Conran, J. G., Lee, W. G., & Lee, D. E. (2019). The presence of moisture deficits in Miocene New Zealand. *Glob. Planet. Change*, 172, 268–277. <https://doi.org/10.1016/j.gloplacha.2018.10.013>

Salpin, M., Schnyder, J., Baudin, F., Suan, G., Suc, J.-P., Popescu, S.-M., et al. (2019). Evidence for subtropical warmth in the Canadian Arctic (Beaufort-Mackenzie, Northwest Territories, Canada) during the early Eocene. [https://doi.org/10.1130/2018.2541\(27\)](https://doi.org/10.1130/2018.2541(27))

Schuster, M., Düringer, P., Ghienne, J.-F., Roquin, C., Sepulchre, P., Moussa, A., et al. (2009). Chad basin: Paleoenvironments of the Sahara since the late Miocene. *Comptes Rendus Geoscience*, 341(8–9), 603–611. <https://doi.org/10.1016/j.crte.2009.04.001>

Seager, R., & Henderson, N. (2013). Diagnostic Computation of moisture budgets in the ERA-interim reanalysis with reference to analysis of CMIP-Archived atmospheric model data. *Journal of Climate*, 26(20), 7876–7901. <https://doi.org/10.1175/JCLI-D-13-00018.1>

Seager, R., Naik, N., & Vecchi, G. A. (2010). Thermodynamic and dynamic mechanisms for large-scale changes in the hydrological cycle in response to global warming. *Journal of Climate*, 23(17), 4651–4668. <https://doi.org/10.1175/2010JCLI3655.1>

Shukla, A., Mehrotra, R. C., Spicer, R. A., Spicer, T. E. V., & Kumar, M. (2014). Cool equatorial terrestrial temperatures and the South Asian monsoon in the Early Eocene: Evidence from the Gurha Mine, Rajasthan, India. *Palaeogeography, Palaeoclimatology, Palaeoecology*, 412, 187–198. <https://doi.org/10.1016/j.palaeo.2014.08.004>

Siler, N., Roe, G. H., Armour, K. C., & Feldl, N. (2019). Revisiting the surface-energy-flux perspective on the sensitivity of global precipitation to climate change. *Climate Dynamics*, 52(7–8), 3983–3995. <https://doi.org/10.1007/s00382-018-4359-0>

Slingo, J., Bates, P., Bauer, P., Belcher, S., Palmer, T., Stephens, G., et al. (2022). Ambitious partnership needed for reliable climate prediction. *Nature Climate Change*, 12(6), 499–503. <https://doi.org/10.1038/s41558-022-01384-8>

Sluijs, A., Bijl, P. K., Schouten, S., Röhl, U., Reichart, G.-J., & Brinkhuis, H. (2011). Southern ocean warming, sea level and hydrological change during the Paleocene-Eocene thermal maximum. *Climate of the Past*, 7(1), 47–61. <https://doi.org/10.5194/cp-7-47-2011>

Smith, F. A., Wing, S. L., & Freeman, K. H. (2007). Magnitude of the carbon isotope excursion at the Paleocene–Eocene thermal maximum: The role of plant community change. *Earth and Planetary Science Letters*, 262(1–2), 50–65. <https://doi.org/10.1016/j.epsl.2007.07.021>

Smith, V., Warny, S., Jarzen, D. M., Demchuk, T., Vajda, V., & Gulick, S. P. S. (2020). Paleocene–Eocene palynomorphs from the Chicxulub impact crater, Mexico. Part 2: Angiosperm pollen. *Palynology*, 44(3), 489–519. <https://doi.org/10.1080/01916122.2019.1705417>

Sniderman, J. M. K., Woodhead, J. D., Hellstrom, J., Jordan, G. J., Drysdale, R. N., Tyler, J. J., & Porch, N. (2016). Pliocene reversal of late Neogene aridification. *Proceedings of the National Academy of Sciences*, 113(8), 1999–2004. <https://doi.org/10.1073/pnas.1520188113>

Spicer, R. A., Yang, J., Spicer, T. E. V., & Farnsworth, A. (2021). Woody dicot leaf traits as a palaeoclimate proxy: 100 years of development and application. *Palaeogeography, Palaeoclimatology, Palaeoecology*, 562, 110138. <https://doi.org/10.1016/j.palaeo.2020.110138>

Su, T., Spicer, R. A., Wu, F.-X., Farnsworth, A., Huang, J., Rio, C. D., et al. (2020). A Middle Eocene lowland humid subtropical “Shangri-La” ecosystem in central Tibet. *Proceedings of the National Academy of Sciences*, 117(52), 32989–32995. <https://doi.org/10.1073/pnas.2012647117>

Suan, G., Popescu, S.-M., Suc, J.-P., Schnyder, J., Fauquette, S., Baudin, F., et al. (2017). Subtropical climate conditions and mangrove growth in Arctic Siberia during the early Eocene. *Geology*, 45(6), 539–542. <https://doi.org/10.1130/G38547.1>

Teodoridis, V., Mazouch, P., Spicer, R. A., & Uhl, D. (2011). Refining CLAMP—Investigations towards improving the Climate Leaf Analysis Multivariate Program. *Palaeogeography, Palaeoclimatology, Palaeoecology*, 299(1–2), 39–48. <https://doi.org/10.1016/j.palaeo.2010.10.031>

Tian, B., & Dong, X. (2020). The double-ITCZ bias in CMIP3, CMIP5, and CMIP6 models based on annual mean precipitation. *Geophysical Research Letters*, 47(8), e2020GL087232. <https://doi.org/10.1029/2020GL087232>

Tierney, J. E., Zhu, J., Li, M., Ridgwell, A., Hakim, G. J., Poulsen, C. J., et al. (2022). Spatial patterns of climate change across the Paleocene–Eocene thermal maximum. *Proceedings of the National Academy of Sciences*, 119(42), e2205326119. <https://doi.org/10.1073/pnas.2205326119>

Trenberth, K. E., & Guillemot, C. J. (1995). Evaluation of the global atmospheric moisture budget as seen from Analyses. *Journal of Climate*, 8(9), 2255–2272. [https://doi.org/10.1175/1520-0442\(1995\)008<2255:EGOTGAM>2.0.CO;2](https://doi.org/10.1175/1520-0442(1995)008<2255:EGOTGAM>2.0.CO;2)

Tripathi, S. K. M., Saxena, R. K., & Prasad, V. (2000). Palynological investigation of the Tura Formation (Early Eocene) exposed along the Tura-Dalu Road, West Garo Hills, Meghalaya, India. *Palaeobotanist*, 49(1–3), 239–252. <https://doi.org/10.5499/jop.2000.145>

van Dijk, J., Fernandez, A., Bernasconi, S. M., Caves Rugenstein, J. K., Passey, S. R., & White, T. (2020). Spatial pattern of super-greenhouse warmth controlled by elevated specific humidity. *Nature Geoscience*, 13(11), 739–744. <https://doi.org/10.1038/s41561-020-00648-2>

Verma, P., Garg, R., Rao, M. R., & Bajpai, S. (2019). Palynofloral diversity and palaeoenvironments of early Eocene Akri lignite succession, Kutch Basin, western India. *Palaeobiodiversity Palaeoenvironments*. <https://doi.org/10.1007/s12549-019-00388-1>

Wang, H., Lu, H., Zhao, L., Zhang, H., Lei, F., & Wang, Y. (2019). Asian monsoon rainfall variation during the Pliocene forced by global temperature change. *Nature Communications*, 10(1), 5272. <https://doi.org/10.1038/s41467-019-13338-4>

West, C. K., Greenwood, D. R., & Basinger, J. F. (2015). Was the Arctic Eocene ‘rainforest’ monsoonal? Estimates of seasonal precipitation from early Eocene megafloras from Ellesmere Island, Nunavut. *Earth and Planetary Science Letters*, 427, 18–30. <https://doi.org/10.1016/j.epsl.2015.06.036>

West, C. K., Greenwood, D. R., Reichgelt, T., Lowe, A. J., Vachon, J. M., & Basinger, J. F. (2020). Paleobotanical proxies for early Eocene climates and ecosystems in northern North America from middle to high latitudes. *Climate of the Past*, 16(4), 1387–1410. <https://doi.org/10.5194/cp-16-1387-2020>

Wiemann, M. C., Wheeler, E. A., Manchester, S. R., & Portier, K. M. (1998). Dicotyledonous wood anatomical characters as predictors of climate. *Palaeogeography, Palaeoclimatology, Palaeoecology*, 139(1–2), 83–100. [https://doi.org/10.1016/S0031-0182\(97\)00100-4](https://doi.org/10.1016/S0031-0182(97)00100-4)

Wilf, P., Wing, S. L., Greenwood, D. R., & Greenwood, C. L. (1998). Using fossil leaves as paleoprecipitation indicators: An Eocene example. *Geology*, 26(3), 203–206. [https://doi.org/10.1130/0091-7613\(1998\)026<203:UFLAPI>2.3.CO;2](https://doi.org/10.1130/0091-7613(1998)026<203:UFLAPI>2.3.CO;2)

Willard, D. A., Donders, T. H., Reichgelt, T., Greenwood, D. R., Sangiorgi, F., Peterse, F., et al. (2019). Arctic vegetation, temperature, and hydrology during Early Eocene transient global warming events. *Global and Planetary Change*, 178, 139–152. <https://doi.org/10.1016/j.gloplacha.2019.04.012>

Williams, C. J. R., Lunt, D. J., Salzmann, U., Reichgelt, T., Inglis, G. N., Greenwood, D. R., et al. (2022). African hydroclimate during the Early Eocene from the DeepMIP simulations. *Paleoceanography and Paleoclimatology*, 37(5), e2022PA004419. <https://doi.org/10.1029/2022PA004419>

Wing, S. L., & Greenwood, D. R. (1993). Fossils and fossil climate: The case for equable continental interiors in the Eocene. *Philosophical Transactions of the Royal Society of London. Series B, Biological Sciences*, 341, 243–252. <https://doi.org/10.1098/rstb.1993.0109>

Wing, S. L., Herrera, F., Jaramillo, C. A., Gómez-Navarro, C., Wilf, P., & Labandeira, C. C. (2009). Late Paleocene fossils from the Cerrejón Formation, Colombia, are the earliest record of Neotropical rainforest. *Proceedings of the National Academy of Sciences*, 106(44), 18627–18632. <https://doi.org/10.1073/pnas.0905130106>

Wolfe, J. A. (1993). *A method of obtaining climatic parameters from leaf assemblages* (p. 360). U.S. Government Printing Office.

Wolfe, J. A. (1995). Paleoclimatic Estimates from tertiary leaf assemblages. *Annual Review of Earth and Planetary Sciences*, 23(1), 119–142. <https://doi.org/10.1146/annurev.ea.23.050195.001003>

Xie, P., & Arkin, P. A. (1997). Global precipitation: A 17-year monthly analysis based on gauge observations, satellite estimates, and numerical model outputs. *Bulletin of the American Meteorological Society*, 78(11), 2539–2558. [https://doi.org/10.1175/1520-0477\(1997\)078<2539:gpyma>2.0.co;2](https://doi.org/10.1175/1520-0477(1997)078<2539:gpyma>2.0.co;2)

Xie, Y., Wu, F., Fang, X., Zhang, D., & Zhang, W. (2020). Early Eocene southern China dominated by desert: Evidence from a palynological record of the Hengyang Basin, Hunan Province. *Global and Planetary Change*, 195, 103320. <https://doi.org/10.1016/j.gloplacha.2020.103320>

Yang, J., Spicer, R. A., Spicer, T. E. V., Arens, N. C., Jacques, F. M. B., Su, T., et al. (2015). Leaf form–climate relationships on the global stage: An ensemble of characters. *Global Ecology and Biogeography*, 24(10), 1113–1125. <https://doi.org/10.1111/geb.12334>

Zhang, R., Yan, Q., Zhang, Z. S., Jiang, D., Otto-Bliesner, B. L., Haywood, A. M., et al. (2013). Mid-Pliocene East Asian monsoon climate simulated in the PlioMIP. *Climate of the Past*, 9(5), 2085–2099. <https://doi.org/10.5194/cp-9-2085-2013>

Zhu, J., Poulsen, C. J., & Tierney, J. E. (2019). Simulation of Eocene extreme warmth and high climate sensitivity through cloud feedbacks. *Science Advances*, 5(9), eaax1874. <https://doi.org/10.1126/sciadv.aax1874>